

Energy & Environmental Science

Accepted Manuscript



This is an *Accepted Manuscript*, which has been through the Royal Society of Chemistry peer review process and has been accepted for publication.

Accepted Manuscripts are published online shortly after acceptance, before technical editing, formatting and proof reading. Using this free service, authors can make their results available to the community, in citable form, before we publish the edited article. We will replace this *Accepted Manuscript* with the edited and formatted *Advance Article* as soon as it is available.

You can find more information about *Accepted Manuscripts* in the [Information for Authors](#).

Please note that technical editing may introduce minor changes to the text and/or graphics, which may alter content. The journal's standard [Terms & Conditions](#) and the [Ethical guidelines](#) still apply. In no event shall the Royal Society of Chemistry be held responsible for any errors or omissions in this *Accepted Manuscript* or any consequences arising from the use of any information it contains.

XAFS Investigation of Polyamidoxime-Bound Uranyl Complexes: the Paradigm from Small Molecule Studies

Received 00th January 20xx,
Accepted 00th January 20xx

C. W. Abney,^{a,b,*} R. T. Mayes,^b M. Piechowicz,^a Z. Lin,^a V. S. Bryantsev,^b G. M. Veith,^b S. Dai,^b and W. Lin^{a,*}

DOI: 10.1039/x0xx00000x

www.rsc.org/

Limited resource availability and population growth have motivated interest in harvesting valuable metals from unconventional reserves, but developing selective adsorbents for this task requires structural knowledge of metal binding environments. Amidoxime polymers have been identified as the most promising platform for large-scale extraction of uranium from seawater. However, despite more than 30 years of research, the uranyl coordination environment on these adsorbents has not been positively identified. We report the first XAFS investigation of polyamidoxime-bound uranyl, with EXAFS fits suggesting a cooperative chelating model, rather than the tridentate or η^2 motifs proposed by small molecule and computational studies. Samples exposed to environmental seawater also display a feature consistent with a μ^2 -oxo-bridged transition metal in the uranyl coordination sphere, suggesting *in situ* formation of a specific binding site or mineralization of uranium on the polymer surface. These unexpected findings challenge several long-held assumptions and have significant implications for development of polymer adsorbents with high selectivity.

Rapid economic growth of emerging countries in conjunction with development of new technologies drives an accelerating demand for a wide range of industrial metals and minerals. Reserves of such non-renewable raw materials are often limited to a few countries, where social and political factors can affect supply security and result in severe global economic repercussions.¹ Uranium is one such “critical metal,” with nuclear fuel applications making its supply certainty a matter of global energy security.² While studies have estimated

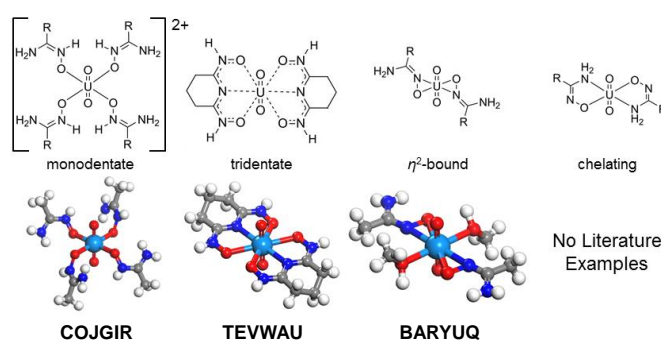


Figure 1: The proposed coordination motifs for how amidoxime binds uranyl, with corresponding crystal structures and CCDC identifiers when available.

terrestrial uranium ores can sustain 100 years of power generation at the current consumption rates,³ more than 1000× this quantity is dissolved in the world’s oceans.⁴ Seawater and industrial wastewater have also been identified as untapped reserves for harvesting valuable resources, including platinum group metals, rare-earth elements, lithium, and copper.⁵ Development of advanced sorbent materials could afford a near-limitless supply of uranium for the nuclear fuel cycle as well as provide the expensive raw materials necessary for industrial manufacturing, achieving a financial backstop and ensuring market stability.⁶ However, attaining these ambitious tasks demands the design of adsorbents with high affinity and selectivity for specific elements

The current state-of-the-art technology for seawater extraction of dioxouranium(VI), otherwise known as uranyl, is an amidoxime-functionalized polymer braid, with recently-reported adsorbents achieving capacities as high as 3.3 g uranium kg⁻¹ adsorbent.⁷ Despite more than three decades of investigation,⁸ the only insights regarding how amidoxime-functionalized polymers bind uranyl have been achieved through small molecule studies and computational investigations. The absence of long-range ordering precludes x-ray diffraction, while low metal content limits the information available through IR, Raman, or x-ray photoelectron spectroscopies (Figures S3-S4 and S17) and differential pair distribution function experiments (Figure S18). Positive identification of the coordination

^aThe University of Chicago, 929 East 57th Street, Chicago, Illinois 60637, United States. E-mail: wenbinlin@uchicago.edu

^bOak Ridge National Laboratory, P.O. Box 2008, Oak Ridge, Tennessee 37831-6181, United States. E-mail: abneycw@ornl.gov

Electronic Supplementary Information (ESI) available: General experimental details; Synthesis and characterization of ligands and small molecule standards; Details regarding XAFS sample preparation and measurements; Description of XAFS fitting; XPS experimental details; PDF experimental details; Computational methods and results; Crystallographic methods and results. Crystal structure available from the CCDC, No. 1419942. See DOI: 10.1039/x0xx00000x

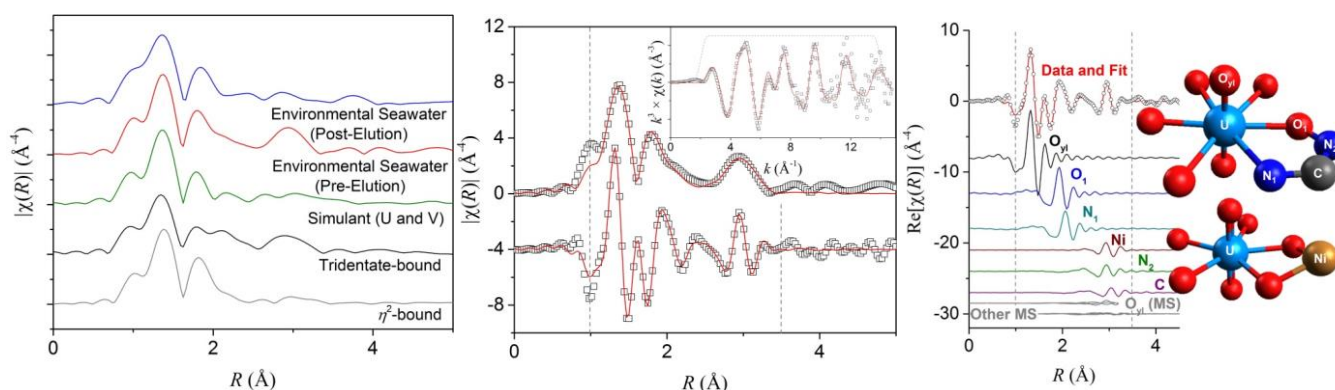


Figure 2. (Left) Direct comparison of uranium L_{III} -edge EXAFS spectra for small molecule standards and amidoxime-functionalized polymer fibres exposed to environmental seawater or seawater simulant. Note the dissimilar features at 2.1 Å and 3 Å of the tridentate-bound small molecule standard. (Centre) Data (squares) and fit (red line) of the polymer fibres exposed to seawater simulant containing uranium and vanadium. The lower plot is the real-space component of the Fourier transform, while the upper plot is the magnitude of the Fourier transform. The grey dashed lines represent the region over which the data were fitted. (Centre, Inset) The corresponding data and fit displayed in k -space. (Right) Data (red line) and fit (open circles) for the real component of the Fourier transform of seawater-contacted polymer fibres, with direct scattering paths from the structure model offset underneath. The data are fit over the range from 1 – 3.5 Å. Major uranyl species are depicted next to each spectrum. Spectra are not phase adjusted.

environment of uranyl is critical for the design of selective ligands and guides understanding of how complex polymer systems behave under non-equilibrium conditions.

The first reported crystal structure of a uranyl-amidoxime complex displayed a coordination motif where four oximes bound the uranium in the equatorial plane (Figure 1).⁹ Subsequent investigations suggested a chelating interaction, where two to three ligands bind uranyl in a bidentate fashion through both the amine and oxime functions.^{10, 11} A seminal work by Vukovic and colleagues leveraged DFT calculations and crystallography to predict an η^2 binding interaction to be most thermodynamically favoured,¹² which was simultaneously reported in amidoxime-functionalized ionic liquid extractants.¹³ More recently, a uranyl bis-amidoxime imidazole crystal structure provided the first instance of a chelating di(oximate) uranyl complex where no tautomerization was observed, suggesting adjacent amidoxime groups could bind uranium in a 2:1 ratio.¹⁴

Early reports also indicated amidoxime installation and subsequent KOH activation processes can result in formation of a cyclic imide dioxime species. It was proposed this functionality would bind more strongly to uranyl and is ultimately responsible for the observed sorption.^{15, 16} Potentiometric titrations supported this assessment, as uranyl bonding by an open-chain diamidoxime was not thermodynamically competitive relative to carbonate in seawater,¹⁷ while the cyclic imide dioxime was observed to form a tridentate complex and bind strongly.¹⁸ It was concluded that formation of cyclic imide dioxime sites should be maximized to improve uranyl uptake.¹⁶⁻¹⁹

In an effort to positively identify the uranyl coordination environment, we have applied X-ray Absorption Fine Structure (XAFS) spectroscopy to investigate amidoxime-functionalized polymer fibres exposed to environmental seawater or seawater simulant. Fits of the extended XAFS (EXAFS) region allow for investigation of the local atomic structure of uranyl and determination of the uranyl binding moiety. While XAFS has been used to investigate uranyl complexes,²⁰⁻²² radiological

waste sediments,²³ biostimulation products,²⁴ and sorption of uranyl by organic ligands,^{25, 26} clays and minerals,²⁷⁻³⁵ amorphous silica,³⁶ biomass,³⁷ and bacteria,³⁸ this is the first instance EXAFS fits have been reported for uranyl bound to amidoxime-functionalized fibres.

Amidoxime-functionalized polymer fibres (hereafter referred to simply as “polymer fibres”) were prepared as reported previously³⁹ and exposed to uranium under several conditions. Two samples of pristine polymer fibres were KOH-treated and exposed for 24 hrs to seawater simulant containing either uranyl nitrate or a combination of uranyl nitrate and sodium orthovanadate.^{7, 40} Two additional fibre samples were investigated after 56 days contact in filtered environmental seawater at Pacific Northwest National Laboratory.⁷ One seawater-contacted sample was investigated as received, while the other was eluted of all metals other than uranium and vanadium.⁴¹ Small molecule standards of uranyl benzamidoxime,¹² and uranyl glutarimidedioxime¹⁸ were synthesized and investigated for comparison, as they possess the proposed η^2 and tridentate motifs, respectively.

XAFS data were collected at the uranium L_{III} -edge (17166 eV) at beamline 10BM-B at the Advanced Photon Source of Argonne National Laboratory,⁴² and processed using the Demeter software suite of the IFEFFIT package based on FEFF 6.^{43, 44} Additional details regarding sample preparation, data collection and processing, fitting, and refinement are provided in the Supporting Information.

Direct comparison of the R -space EXAFS spectra reveals distinct differences among the five samples (Figure 2). Most specifically, the small molecule standard with the tridentate-binding mode possesses a peak at approximately 2.2 Å which is not present in any of the other spectra, as well as a broad peak at 3 Å. Deconvolution of the calculated scattering paths responsible for these features reveal they are attributable to direct scattering off the imine nitrogen (2.2 Å) and the combination of direct scattering from oxime N and C as well as multiple scattering from the axial O on uranyl (3 Å) (Figure S6).

Table 1 EXAFS fits for amidoxime-functionalized polymer fibres exposed to seawater simulant with uranium and vanadium or environmental seawater

Seawater Simulant

Path	Coord. No.	Bond Length (Å)	σ^2 ($\times 10^{-3} \text{ \AA}^2$)
U \rightarrow O _{yl}	2	1.80 \pm 0.01	2 \pm 0.3
U \rightarrow O	3.1 \pm 0.7	2.35 \pm 0.02	6 \pm 2
U \rightarrow N ₁	3.1 \pm 0.7	2.49 \pm 0.02	6 \pm 2
U \rightarrow N ₂	3.4 \pm 1.1	3.37 \pm 0.04	6 \pm 2
U \rightarrow C	3.4 \pm 1.1	3.48 \pm 0.02	2 \pm 1
U \rightarrow O \rightarrow N ₂	3.1 \pm 0.7	3.59 \pm 0.02	4 \pm 2
U \rightarrow O _{yl} \rightarrow O	6.2 \pm 0.5	3.59 \pm 0.01	3 \pm 1
U \rightarrow O _{yl(1)} \rightarrow O _{yl(2)}	2	3.61 \pm 0.01	4 \pm 1
U \rightarrow O _{yl(1)} \rightarrow U \rightarrow O _{yl(1)}	2	3.61 \pm 0.01	4 \pm 1
U \rightarrow O _{yl(1)} \rightarrow U \rightarrow O _{yl(2)}	2	3.61 \pm 0.01	4 \pm 1

Environmental Seawater

Path	Coord. No.	Bond Length (Å)	σ^2 ($\times 10^{-3} \text{ \AA}^2$)
U \rightarrow O _{yl}	2	1.80 \pm 0.01	2 \pm 0.3
U \rightarrow O ₁	2.8 \pm 0.6	2.40 \pm 0.02	3 \pm 2
U \rightarrow N ₁	2.8 \pm 0.6	2.56 \pm 0.02	3 \pm 2
U \rightarrow N ₂	2.2 \pm 0.2	3.41 \pm 0.07	3 \pm 2
U \rightarrow C	2.2 \pm 0.2	3.54 \pm 0.07	3 \pm 2
U \rightarrow Ni	1 \pm 1	3.41 \pm 0.04	6 \pm 4
U \rightarrow O ₁ \rightarrow N ₂	2.8 \pm 0.3	3.59 \pm 0.04	4 \pm 2
U \rightarrow O _{yl(1)} \rightarrow O _{yl(2)}	2	3.61 \pm 0.01	4 \pm 1
U \rightarrow O _{yl(1)} \rightarrow U \rightarrow O _{yl(1)}	2	3.61 \pm 0.01	4 \pm 1
U \rightarrow O _{yl(1)} \rightarrow U \rightarrow O _{yl(2)}	2	3.61 \pm 0.01	4 \pm 1
U \rightarrow O _{yl} \rightarrow N ₁	5.6 \pm 0.3	3.70 \pm 0.01	4 \pm 1
U \rightarrow O _{yl} \rightarrow O ₁	5.6 \pm 0.3	3.70 \pm 0.01	4 \pm 1
U \rightarrow N ₁ \rightarrow C	5.6 \pm 0.3	3.72 \pm 0.01	4 \pm 2

Polymer fibres exposed to seawater simulant were fit by a model composed of three shells of scattering elements (Figures S10, S12). Two axial O of uranyl (O_{yl}) comprise the first shell, with their coordination number fixed. The second shell contains a variable number of O and N with different path lengths, while the third shell consists of a variable number of N and C, each with a different path length. Inclusion of carbonate scattering features were attempted during fits for all samples, but were never observed to contribute to a statistically significant extent as determined by the Hamilton Test.^{45, 46}

The equatorial coordination environment of uranyl consists of 5.6 \pm 1.2 (U only, Table S9) or 6.2 \pm 1.4 (U and V, Table 1) light scattering elements, while the third shell contains 2.8 \pm 1.2 of both N and C (U only) or 3.4 \pm 1.1 of both N and C (U and V). While the identity of these light scatterers cannot be directly obtained by EXAFS,⁴⁷ these coordination numbers and bond lengths are consistent with the average local atomic environment of uranyl containing 2-3 amidoximes binding in a chelating fashion. Six equatorially-coordinating atoms is common for uranyl complexes, such as uranyl carbonate, and computational findings suggest solvation of uranyl with 5 or 6 water molecules is isoenergetic.⁴⁸ Equatorial coordination by 5 atoms could result from two chelating amidoximes and one monodentate-bound ligand. X-ray photoelectron spectroscopy measurements performed on a uranium-saturated amidoxime-

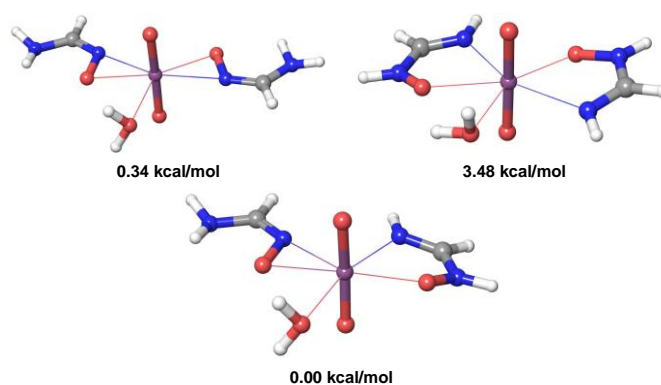


Figure 3 Structures of uranyl complexes with formamidoxime obtained after geometry optimization at the B3LYP/SSC/6-311++G(d,p) level of theory. Relative stabilities for the complexes calculated with coupled cluster corrections at the CCSD(T) level are displayed below. Results are consistent with those obtained for MP2 optimized geometries, provided in the Supporting Information.

functionalized polyethylene membrane prepared similarly to the fibrous adsorbent indicate this may be attributable to U-OH or U-O-Na (Figure S17), though monodentate-bound amidoxime or carboxylic acid could also be contributors.⁴⁹

This proposed chelating motif conflicts with recent density functional theory (DFT) work, which indicates the η^2 motif is thermodynamically preferred.¹² However, in the aforementioned study, the calculated energies for chelating amidoxime were only 3 kcal mol⁻¹ less favoured in most instances.¹² Additional calculations performed in this work for uranyl bound by one formamidoxime reveal differences of approximately 0-2 kcal mol⁻¹ after applying a correction of the coupled cluster theory with simple, double, and perturbative triple excitations (CCSD(T)) in the *aug-cc-pVDZ* basis set (Table S16). Moreover, a five-coordinate 1:2 uranyl complex with mixed coordination of the two ligands is slightly more stable than that with pure η^2 coordination at the CCSD(T) level (Figure 3). Additionally, recent failed sorption efforts with oxime-functionalized polymers reveal the non-innocence of the adjacent amine,⁵⁰ which cannot be readily explained by an η^2 bonding motif⁵¹ and is more consistent with uranyl chelation. It is also important to acknowledge that small molecule and computational studies with isolated ligands may not be accurate representations of complex amorphous heterogeneous materials under non-equilibrium conditions. While a reasonable fit can also be achieved using a model representative of an η^2 motif, comparison of R-factor and χ_v^2 metrics indicate the chelating model is better fitted to the experimental spectra (Figure S11).⁴⁶ Nevertheless, the η^2 motif cannot be unequivocally discounted. In contrast, a model representative of tridentate cyclic imidioxime binding does not fit the data well, resulting in significant distortion of bond lengths from the crystalline standard, large errors, and higher R-factor and χ_v^2 metrics (Figure S14).

The first and second shells of the EXAFS spectra for the environmental seawater-contacted polymer fibres are fit in a manner identical to the previous samples (Table 1). The first shell consists of the O_{yl} scattering paths, while 2.8 \pm 0.6 oxygen and an equivalent number of nitrogen comprise the second

shell. Bond lengths and coordination numbers for these paths are consistent with literature data.²⁵ However, a large scattering contribution at 3 Å in R-space, similar to the spectrum of the tridentate-binding cyclic imide dioxime, cannot be readily fit with a chelating model. When fit with only light scattering elements (C, N, O, P) in the third shell, physically unreasonable coordination numbers (> 8) are required to model the spectra. Comparison of EXAFS data at different k-weights (Figure S15) reveals the feature at 3 Å grows in dramatically with increasing k-weight, consistent with scattering from a heavier element. Introduction of a μ^2 -oxo bridged metal is necessary to achieve sufficient scattering intensity at this distance. Such a phenomenon is plausible, as several transition metals are known to be extracted from seawater in amounts equal or greater than uranium,^{7, 52} and uranyl μ^2 -oxo Cu, Fe, Zn, U, and V complexes are reported in the literature.⁵³⁻⁵⁹ While Ca, Na, and Mg are all extracted in greater quantities than the transition metals,^{7, 52} and uranyl carbonate complexes with Ca and Na have been identified previously,^{20, 60, 61} their scattering contributions occur from 3.8 – 4.1 Å and are outside of the range considered by the fit.[‡]

Analysis of the polymer fibres after treatment with dilute HCl reveals a dramatic reduction in the intensity of the feature at 3 Å in R-space (Figure 2, Figure S13, S16). As acid treatment is known to elute most transition metals, this result is consistent with the assignment of a μ^2 -oxo bridged metal in the third shell of the seawater-contacted polymer fibres. ICP-MS analysis of the post-eluted fibres reveals minimal change in Cu, V, and U concentrations, but significant reduction in Fe, Ni, and Zn (Table S2). The reduction in feature intensity despite Cu, V, and U persistence suggests scattering off these metals is not the main contribution to the feature at 3 Å. This is also in agreement with spectra and fits for polymer fibres contacted with U and V in seawater simulant.

Based on reported single crystal data, we propose a Ni scatterer to be the most likely contributor in this region due to having an appropriate U-Ni bond length around 3.5 Å.⁶² Inclusion of a Ni scattering path yields a third shell containing 4.4 ± 0.4 light scatterers and 1 ± 1 Ni (Table 1), consistent with two chelating amidoximes and one μ^2 -oxo bridged metal. Similar results can also be obtained with Fe or Zn, though their bond lengths are longer in reported crystal structures.^{54, 55} The large error is likely due to the averaging of multiple different uranyl μ^2 -oxo bridged metal scattering paths in the spectra, as well as contributing to the same spectral region as phosphate and the third shell scatterers of chelating amidoximes.

Finally, efforts to fit seawater contacted fibres using models representative of η^2 -bound amidoxime or tridentate-bound cyclic imide dioxime were unsuccessful, regardless of whether μ^2 -oxo bridged metal, carbonate, or phosphate scattering paths were included. Consistent with previously reported chemical instability⁶³ and over 25 years devoid of any publications reporting further development,¹⁶ there is no evidence to support the binding of uranyl by cyclic imide dioximes.

Conclusions

A series of uranyl-contacted amidoxime-functionalized polymer fibres were analysed by EXAFS to investigate the amidoxime bonding motif. In seawater simulant, the local atomic coordination environment was most consistent with chelation by 2-3 amidoxime functionalities, with computational results indicating two cooperating ligands to be most defensible thermodynamically. While also consistent with binding by two chelating ligands, spectra for seawater contacted fibres could not be fit without inclusion of a uranyl μ^2 -oxo Ni scattering path, though the precise identity of the transition metal cannot be directly confirmed. None of the spectra could be well-fitted using a tridentate-binding cyclic imide dioxime model, and while the proposed η^2 motif was able to fit the simulant-contacted fibres, it is disfavoured on the basis of *a priori* knowledge, statistical analysis, and further computational investigation.

Beyond simply identifying the uranyl bonding environment, the implications for these findings are significant and challenge several long-held assumptions. In order to obtain the coordination environment revealed by EXAFS fits, multiple amidoxime functionalities must bind one uranyl, invalidating the paradigm of single-ligand binding and requiring updated models for the analysis of these complex systems. Cooperative binding requires at least two functionalities to interact with uranyl, suggesting polymer conformation may influence sorption capacity more significantly than previously considered. Structure-based uranyl sorbents exploiting this “cooperative binding,” such as porous polymers,⁶⁴ metal-organic frameworks,⁶⁵ or engineered proteins,⁶⁶ have been previously reported and may thus merit further investigation.⁶⁷ Furthermore, the μ^2 -oxo bridged transition metal observed on seawater-contacted fibres indicates an entirely different atomic environment exists for seawater-extracted uranyl, explaining in part the dramatic reduction in capacity between studies performed in simulant vs. environmental seawater. Small molecule complexes have been reported which possess not only this close U-Ni distance, but also display a coordination environment consistent with the best-fit model for seawater-contacted fibres.⁶² It is possible uranyl sorption in seawater occurs only after *in situ* formation of an advantageous binding pocket by chelating Ni or another transition metal. Similar behaviour has been reported in metallacrown complexes,^{68, 69} and leveraging this novel approach could enable entirely new regimes for ligand design and adsorbent engineering.

Acknowledgements

This research was conducted at the University of Chicago and Oak Ridge National Laboratory (ORNL). Work at the University of Chicago was supported by the U.S. Department of Energy (DOE) Office of Nuclear Energy’s Nuclear Energy University Program (Sub-Contract – 20 #120427, Project #3151). Work at ORNL was sponsored by the U.S. DOE,

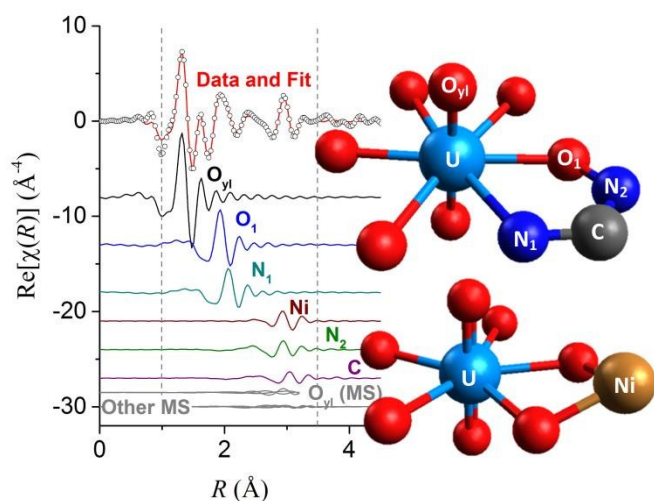
Office of Nuclear Energy. XAFS data were collected at the Advanced Photon Source at Argonne National Laboratory on Beamline 10BM-B, supported by the Materials Research Collaborative Access Team (MRCAT). MRCAT operations are supported by the DOE and the MRCAT member institutions. Pair distribution function data were collected at the Advanced Photon Source on Beamline 11ID-B, supported by the X-ray Sciences, Structural Sciences Division. The Advanced Photon Source is a U.S. DOE Office of Science User Facility operated for the DOE Office of Science by Argonne National Laboratory under Contract No. DE-AC02-06CH11357. This research used resources of the National Energy Research Scientific Computing Centre, a DOE Office of Science User Facility supported by the Office of Science of the U.S. DOE under Contract No. DE-AC02-05CH11231. The authors thank Dr. Gary Gill from Pacific Northwest National Laboratory for providing the seawater-contacted polymer fibres, and Dr. Alex Filatov from the University of Chicago for assistance with crystallographic refinement and reporting. The authors also thank the University of Chicago Physical Science Division Mass Spectrometry, NMR, and Crystallography Facilities, as well as the NSF Materials Research Science and Engineering Center (MRSEC) at the University of Chicago for instrumentation.

Notes and references

‡ The EXAFS signal depends on $\sin[2kR_i + \delta_i(k)]$, where k is the energy of the photoelectron in wavenumbers, R is the half-path length of the i th scatterer, and $\delta_i(k)$ is the phase shift of the photoelectron. In this work we generally refer to the crystallographic positions of the atoms in terms of their actual distance in Å from uranium. However, their contributions to the Fourier transform of the data are discussed in terms of their distance in Å, uncorrected for $\delta_i(k)$. As a result, plots of the Fourier transform display features attributable to atoms which are approximately 0.5 Å farther away than is indicated by the x-axis. Thus, half-path lengths (i.e. bond lengths) of approximately 3.5 Å are most reasonable for generating a feature at 3 Å in R-space.

1. S. Glöser, L. Tercero Espinoza, C. Gandenberger and M. Faulstich, *Resources Policy*, 2015, **44**, 35-46.
2. S. F. Ashley, R. A. Fenner, W. J. Nuttall and G. T. Parks, *Energy Convers. Manage.*, 2015, **101**, 136-150.
3. OECD, *Uranium 2014: Resources, Production, and Demand*, 2014.
4. R. V. Davies, J. Kennedy, R. W. McIlroy, R. Spence and K. M. Hill, *Nature*, 1964, **203**, 1110-1115.
5. M. S. Diallo, M. R. Kotte and M. Cho, *Environ. Sci. Technol.*, 2015, DOI: 10.1021/acs.est.5b00463.
6. H. Lindner and E. Schneider, *Energy Economics*, 2015, **49**, 9-22.
7. J. Kim, C. Tsouris, Y. Oyola, C. J. Janke, R. T. Mayes, S. Dai, G. Gill, L.-J. Kuo, J. Wood, K.-Y. Choe, E. Schneider and H. Lindner, *Ind. Eng. Chem. Res.*, 2014, **53**, 6076-6083.
8. H. J. Schenk, L. Astheimer, E. G. Witte and K. Schwochau, *Sep. Sci. Technol.*, 1982, **17**, 1293-1308.
9. E. G. Witte, K. S. Schwochau, G. Henkel and B. Krebs, *Inorg. Chim. Acta*, 1984, **94**, 323-331.
10. S. Katragadda, H. D. Gesser and A. Chow, *Talanta*, 1997, **45**, 257-263.
11. A. Zhang, T. Asakura and G. Uchiyama, *React. Funct. Polym.*, 2003, **57**, 67-76.
12. S. Vukovic, L. A. Watson, S. O. Kang, R. Custelcean and B. P. Hay, *Inorg. Chem.*, 2012, **51**, 3855-3859.
13. P. S. Barber, S. P. Kelley and R. D. Rogers, *RSC Adv.*, 2012, **2**, 8526-8530.
14. S. P. Kelley, P. S. Barber, P. H. K. Mullins and R. D. Rogers, *Chem. Commun.*, 2014, **50**, 12504-12507.
15. L. Astheimer, H. J. Schenk, E. G. Witte and K. Schwochau, *Sep. Sci. Technol.*, 1983, **18**, 307-339.
16. Y. Kobuke, H. Tanaka and H. Ogoshi, *Polym J*, 1990, **22**, 179-182.
17. G. Tian, S. Teat and L. Rao, *Dalton. Trans.*, 2013, **42**, 5690-5696.
18. G. Tian, S. Teat, Z. Zhang and L. Rao, *Dalton. Trans.*, 2012, **41**, 11579-11586.
19. F. Endrizzi, A. Melchior, M. Tolazzi and L. Rao, *Dalton. Trans.*, 2015, **44**, 13835-13844.
20. S. D. Kelly, K. M. Kemner and S. C. Brooks, *Geochim. Cosmochim. Acta*, 2007, **71**, 821-834.
21. P. G. Allen, J. J. Bucher, D. L. Clark, N. M. Edelstein, S. A. Ekberg, J. W. Gohdes, E. A. Hudson, N. Kaltsayannis and W. W. Lukens, *Inorg. Chem.*, 1995, **34**, 4797-4807.
22. P. G. Allen, J. J. Bucher, D. K. Shuh, N. M. Edelstein and T. Reich, *Inorg. Chem.*, 1997, **36**, 4676-4683.
23. Y. Arai, M. A. Marcus, N. Tamura, J. A. Davis and J. M. Zachara, *Environ. Sci. Technol.*, 2007, **41**, 4633-4639.
24. S. D. Kelly, K. M. Kemner, J. Carley, C. Criddle, P. M. Jardine, T. L. Marsh, D. Phillips, D. Watson and W.-M. Wu, *Environ. Sci. Technol.*, 2008, **42**, 1558-1564.
25. C. Den Auwer, C. Lecouteux, M. C. Charbonnel, C. Madić and R. Guillaumont, *Polyhedron*, 1997, **16**, 2233-2238.
26. K. Schmeide, S. Sachs, M. Bubner, T. Reich, K. H. Heise and G. Bernhard, *Inorg. Chim. Acta*, 2003, **351**, 133-140.
27. A. J. Dent, J. D. F. Ramsay and S. W. Swanton, *J. Colloid Interface Sci.*, 1992, **150**, 45-60.
28. C. Chisholm-Brause, S. D. Conradson, C. T. Buscher, P. G. Eller and D. E. Morris, *Geochim. Cosmochim. Acta*, 1994, **58**, 3625-3631.
29. J. R. Bargar, R. Reitmeyer and J. A. Davis, *Environ. Sci. Technol.*, 1999, **33**, 2481-2484.
30. L. N. Moyes, R. H. Parkman, J. M. Charnock, D. J. Vaughan, F. R. Livens, C. R. Hughes and A. Braithwaite, *Environ. Sci. Technol.*, 2000, **34**, 1062-1068.
31. J. G. Catalano and G. E. Brown Jr, *Geochim. Cosmochim. Acta*, 2005, **69**, 2995-3005.
32. E. Ordoñez-Regil, R. Drot, E. Simoni and J. J. Ehrhardt, *Langmuir*, 2002, **18**, 7977-7984.
33. D. M. Singer, K. Maher and G. E. Brown Jr, *Geochim. Cosmochim. Acta*, 2009, **73**, 5989-6007.
34. S. Chakraborty, F. Favre, D. Banerjee, A. C. Scheinost, M. Mullet, J.-J. Ehrhardt, J. Brendle, L. Vidal and L. Charlet, *Environ. Sci. Technol.*, 2010, **44**, 3779-3785.
35. A. Walshe, Pru, T. Vitova and R. J. Baker, *Dalton. Trans.*, 2014, **43**, 4400-4407.
36. M. S. Massey, J. S. Lezama-Pacheco, J. M. Nelson, S. Fendorf and K. Maher, *Environ. Sci. Technol.*, 2014, **48**, 8636-8644.
37. J. G. Parsons, K. J. Tiemann, J. R. Peralta-Videa and J. L. Gardea-Torresdey, *Environ. Sci. Technol.*, 2006, **40**, 4181-4188.
38. S. D. Kelly, K. M. Kemner, J. B. Fein, D. A. Fowle, M. I. Boyanov, B. A. Bunker and N. Yee, *Geochim. Cosmochim. Acta*, 2002, **66**, 3855-3871.

39. H.-B. Pan, W. Liao, C. M. Wai, Y. Oyola, C. J. Janke, G. Tian and L. Rao, *Dalton. Trans.*, 2014, **43**, 10713-10718.
40. J. Kim, Y. Oyola, C. Tsouris, C. R. Hexel, R. T. Mayes, C. J. Janke and S. Dai, *Ind. Eng. Chem. Res.*, 2013, **52**, 9433-9440.
41. N. Suzuki, D. Yamamoto, N. Anaguchi, H. Tsuchiya, K. Aoki and Y. Kanzaki, *Bull. Chem. Soc. Jpn.*, 2000, **73**, 2599-2603.
42. A. J. Kropf, J. Katsoudas, S. Chattopadhyay, T. Shibata, E. A. Lang, V. N. Zyryanov, B. Ravel, K. McIvor, K. M. Kemner, K. G. Scheckel, S. R. Bare, J. Terry, S. D. Kelly, B. A. Bunker and C. U. Segre, *AIP Conf. Proc.*, 2010, **1234**, 299-302.
43. B. Ravel and M. Newville, *J. Synchrotron Radiat.*, 2005, **12**, 537-541.
44. J. J. Rehr and R. C. Albers, *Rev. Mod. Phys.*, 2000, **72**, 621-654.
45. W. C. Hamilton, *Acta Crystallographica*, 1965, **18**, 502-510.
46. S. Calvin, *XAFS for Everyone*, CRC Press, Boca Raton, FL, 2013.
47. M. A. Denecke, T. Reich, M. Bubner, S. Pompe, K. H. Heise, H. Nitsche, P. G. Allen, J. J. Bucher, N. M. Edelstein and D. K. Shuh, *J. Alloys Compd.*, 1998, **271-273**, 123-127.
48. M. A. Lashley, N. Mehio, J. W. Nugent, E. Holguin, C.-L. Do-Thanh, V. S. Bryantsev, S. Dai and R. D. Hancock, *Submitted*, 2015.
49. C. Den Auwer, E. Simoni, S. Conradson and C. Madic, *Eur. J. Inorg. Chem.*, 2003, **2003**, 3843-3859.
50. C. Zhang, R. T. Mayes, V. S. Bryantsev and S. Dai, unpublished work.
51. C. W. Abney, S. Liu and W. Lin, *J. Phys. Chem. A*, 2013, **117**, 11558-11565.
52. J. Kim, C. Tsouris, R. T. Mayes, Y. Oyola, T. Saito, C. J. Janke, S. Dai, E. Schneider and D. Sachde, *Sep. Sci. Technol.*, 2013, **48**, 367-387.
53. L. Mandal, S. Bhattacharya and S. Mohanta, *Inorg. Chim. Acta*, 2013, **406**, 87-94.
54. M. Basile, D. K. Unruh, E. Flores, A. Johns and T. Z. Forbes, *Dalton. Trans.*, 2015, **44**, 2597-2605.
55. L. Salmon, P. Thuery and M. Ephritikhine, *Journal*, 2006.
56. Ajay K. Sah, Chebrolu P. Rao, Pauli K. Saarenketo, Elina K. Wegelius, E. Kolehmainen and K. Rissanen, *Eur. J. Inorg. Chem.*, 2001, **2001**, 2773-2781.
57. D. L. Perry, H. Ruben, D. H. Templeton and A. Zalkin, *Inorg. Chem.*, 1980, **19**, 1067-1069.
58. L. Jouffret, M. Rivenet and F. Abraham, *J. Solid State Chem.*, 2010, **183**, 84-92.
59. G. A. Senchyk, E. M. Wylie, S. Prizio, J. E. S. Szymanowski, G. E. Sigmon and P. C. Burns, *Chem. Commun.*, 2015, **51**, 10134-10137.
60. S. Kerisit and C. Liu, *Geochim. Cosmochim. Acta*, 2010, **74**, 4937-4952.
61. F. Endrizzi and L. Rao, *Chem. Eur. J.*, 2014, **20**, 14499-14506.
62. L. Salmon, P. Thuéry and M. Ephritikhine, *Polyhedron*, 2003, **22**, 2683-2688.
63. S. O. Kang, S. Vukovic, R. Custelcean and B. P. Hay, *Ind. Eng. Chem. Res.*, 2012, **51**, 6619-6624.
64. Y. Yue, R. T. Mayes, J. Kim, P. F. Fulvio, X.-G. Sun, C. Tsouris, J. Chen, S. Brown and S. Dai, *Angew. Chem. Int. Ed.*, 2013, **52**, 13458-13462.
65. M. Carboni, C. W. Abney, S. Liu and W. Lin, *Chem. Sci.*, 2013, **4**, 2396-2402.
66. L. Zhou, M. Bosscher, C. Zhang, S. Özçubukçu, L. Zhang, W. Zhang, C. J. Li, J. Liu, M. P. Jensen, L. Lai and C. He, *Nat. Chem.*, 2014, **6**, 236-241.
67. Y. Lu, *Nat. Chem.*, 2014, **6**, 175-177.
68. A. J. Stemmler, J. W. Kampf and V. L. Pecoraro, *Angew. Chem. Int. Ed.*, 1996, **35**, 2841-2843.
69. T. N. Parac-Vogt, A. Pacco, P. Nockemann, Y.-F. Yuan, C. Görrler-Walrand and K. Binnemans, *Eur. J. Inorg. Chem.*, 2006, **2006**, 1466-1474.

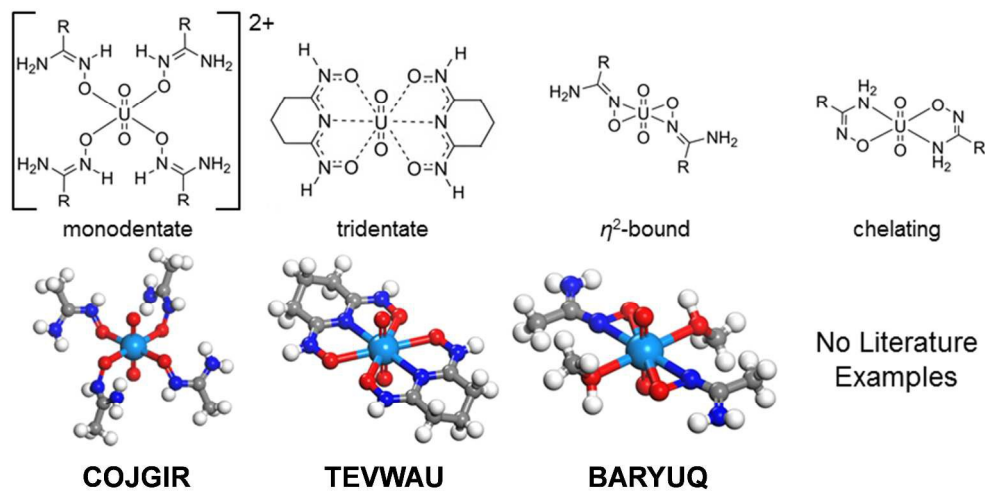


TOC Graphic

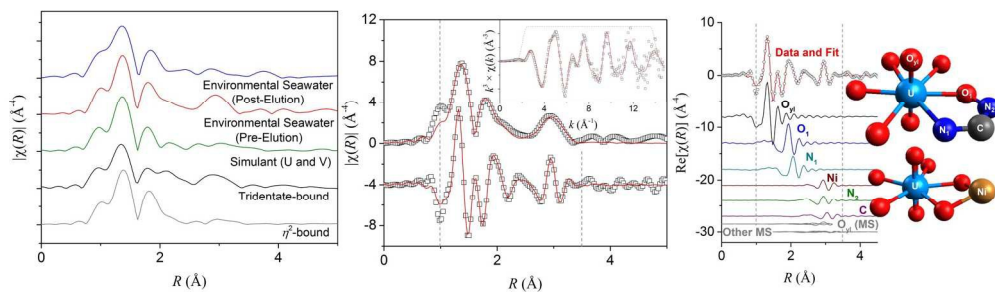
“XAFS investigation of polyamidoxime-bound uranyl reveals an adjacent μ^2 -oxo-bridged transition metal, suggesting new routes for adsorbent design in radionuclide separations.”

Broader Context

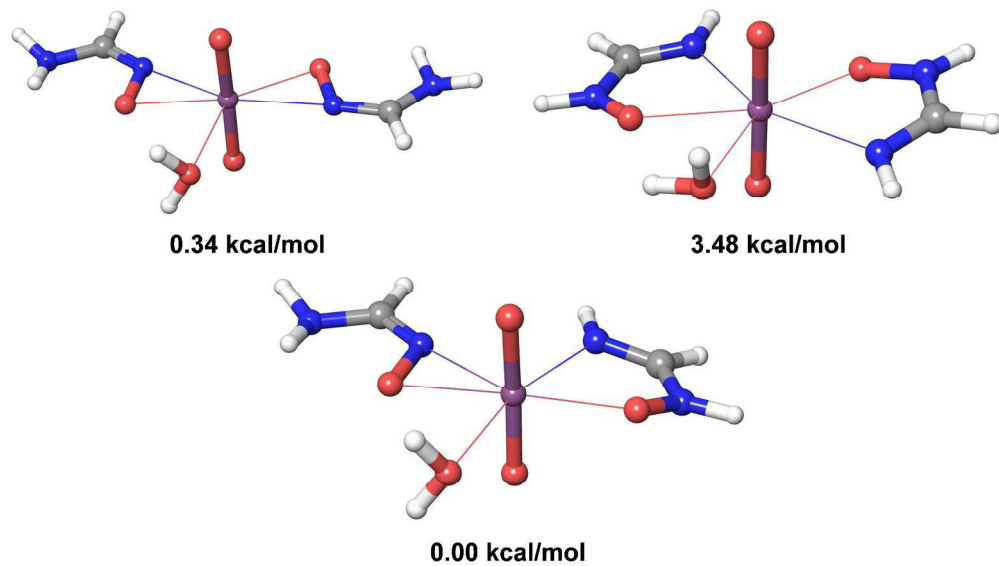
Nuclear energy is the only mature, low-carbon source for base-load power generation. With increasing global energy demand, nuclear power is expected to grow over the coming decades. While the current nuclear fuel source – uranium – is extracted from terrestrial ores, limited global reserves motivate utilization of unconventional sources. In this work we investigate how uranium is bound on an amidoxime-functionalized polymer, the current state-of-the-art technology for extracting uranium from seawater. Our findings challenge the long-held assumption that uranium and amidoxime participate in 1:1 binding, and also reveal that previously reported small molecule studies did not accurately represent uranium binding on the polymer. Notably, the presence of an adjacent μ^2 -oxo-bridging transition metal was unexpected and suggests sorption occurs by mineralization or after *in situ* formation of an advantageous binding pocket. Neither mechanism had been considered previously. This observation may enable new routes for material design, and will guide engineering of solid phase sorbents for applications related to environmental remediation and nuclear waste processing. Furthermore, successful development of adsorbent technologies capable of economical ocean mining would enable a near inexhaustible reserve for numerous critical metals, while doing so with a dramatically lower environmental impact than traditional mining operations.



1405x700mm (96 x 96 DPI)



1488x434mm (96 x 96 DPI)



1587x904mm (96 x 96 DPI)

Supporting Information for: XAFS Investigation of Polyamidoxime-Bound Uranyl Contests the Paradigm from Small Molecule Studies

C. W. Abney,^{a,b*} R. T. Mayes,^b M. Piechowicz,^a Z. Lin,^a V. S. Bryantsev,^b G. M. Veith,^b S. Dai,^b and W. Lin^{a*}

^a The University of Chicago, 929 East 57th Street, Chicago, Illinois 60637, United States

^b Oak Ridge National Laboratory, P.O. Box 2008, Oak Ridge, Tennessee 37831-6181, United States

abneycw@ornl.gov

wenbinlin@uchicago.edu

<u>Section</u>	<u>Page</u>
1. Experimental.....	2
2. Low-Energy Spectroscopy.....	9
3. X-ray Absorption Spectroscopy.....	10
4. X-ray Absorption Near Edge Structure Analysis and Linear Combination Fitting.....	12
5. EXAFS Fitting.....	15
6. X-ray Photoelectron Spectroscopy.....	33
7. Differential Pair Distribution Function.....	34
8. Computational Investigation.....	35
9. Crystallography.....	38
10. References.....	41

1. Experimental

1.1 General Experimental

All chemicals were obtained from Fisher Scientific or Sigma Aldrich. Uranyl acetate dihydrate was obtained from Ted Pella, Inc. and used without purification as a standard, as well as to prepare uranyl nitrate according to a literature procedure.¹ All other chemicals and solvents were used without further purification or treatment. Pristine amidoxime-functionalized polymer fibres prepared by RIGP² were obtained from ORNL. Amidoxime-functionalized polymer fibres, originally prepared at ORNL, were obtained from PNNL after 1 hr KOH activation and 56 days exposure to filtered seawater from the Sequim Bay.^{3,4} Details pertaining to the KOH activation procedure are provided in section 3.2.3.1.

¹H NMR spectra were recorded on a Bruker NMR 500 DRX spectrometer at 500 MHz and referenced to the proton resonance resulting from incomplete deuteration of the CDCl₃ (δ 7.26) or DMSO-*d*₆ (δ 2.50). Thermogravimetric analyses (TGA) were performed in air using a Shimadzu TGA-50H equipped with a platinum pan, heated at 2 °C per minute until 300 °C, then at 10 °C per minute until 600°C. Powder X-ray diffraction (PXRD) was performed on a Bruker D8 X-ray diffractometer using Cu radiation and equipped with a sensitive area detector. ICP-MS data were obtained with an Agilent 7700x ICP-MS and analyzed using ICP-MS MassHunter version B01.03. Samples were diluted in a 2% HNO₃ matrix and analyzed with a ²⁰⁷Bi internal standard against a six-point standard curve over the range from 0.1 ppb to 1000 ppb. The correlation coefficient was > 0.9997 for all analyses of interest. Data collection was performed in Spectrum Mode with five replicates per sample and 100 sweeps per replicate. Raman spectra were collected on a Horiba LabRamHR Evolution confocal Raman microscope with a laser wavelength of 633 nm. Total Attenuated Reflectance-FTIR (ATR-IR) spectra of seawater-contacted fibres were collected with a Thermo Nicolet Nexus 670 FT-IR with ATR attachment. ATR-IR spectra of pristine fibres and simulant-contacted fibres were collected with a Perkin Elmer Frontier FTIR with a single-bounce diamond attenuated total reflectance accessory.

X-ray photoelectron spectroscopy (XPS) data were collected using a PHI 3056 spectrometer with an Al anode source operated at 15 kV and an applied power of 350 W. Adventitious carbon was used to

calibrate the binding energy shifts of the sample $C1s = 284.8$ eV. High resolution data was collected at pass energy of 5.85 eV with 0.05 eV step sizes and a minimum of 60 scans to improve the signal to noise ratio; lower resolution survey scans were collected at pass energy of 93.5 eV with 0.5 eV step sizes and a minimum of 25 scans.

1.2 Synthesis of Small Molecule Standards

1.2.1 Synthesis of Benzamidoxime Benzamidoxime was prepared following a slightly modified protocol from the literature.^{5, 6} In a 25-mL round-bottom flask, 1 g (1 mL, 9.7 mmol) benzonitrile was combined with 0.96 g hydroxylamine (50% in water) (1.5 e.q, 0.89 mL, 14.55 mmol). To this slurry, 10 mL ethanol were added with stirring. The solution was refluxed at 80 °C and monitored by thin-layer chromatography. After 24 hr of reflux, the solution was cooled to room temperature. The solvent was concentrated under vacuum, 10 mL water were added, and the product was extracted three times with CH_2Cl_2 . The organic phase was dried with $MgSO_4$ and the solvent removed under vacuum to yield the crude product. The pure product was obtained following chromatographic purification in 1:1 EtOAc: CH_2Cl_2 , yielding 1.14 g (8.4 mmol, 87% yield) of a white crystalline solid. The 1H NMR spectra was confirmed against the spectra available in the literature.

1.2.2 Synthesis of Glutarimidedioxime Glutarimidedioxime was prepared following a slightly modified protocol from the literature.⁷ In a 100-mL glass pressure vessel with threaded Teflon cap, 5 mL EtOH and 6 mL H_2O were combined. 872 mg NaOH (21.8 mmol) were added and stirred until fully dissolved. 1.556 g $NH_2OH \cdot HCl$ (21.8 mmol) were gradually added over 15 minutes with stirring, allowing full dissolution before further addition. 500 μL (5.26 mmol) glutaronitrile was added by syringe. The vessel was sealed with the Teflon cap, immersed in oil, and heated at 85 °C with stirring. After 5 days, the vessel was removed from heat and allowed to cool naturally to room temperature. White precipitate was observed as the reaction solution cooled. 170 mg fibrous white solid was collected by filtration (1.19 mmol, 5.5% yield). The 1H NMR spectra was confirmed against the spectra available in the literature.

1.2.3 Preparation of Uranyl Benzamidoxime Crystals Single crystals of $\text{UO}_2(\text{Benzamidoximate})_2(\text{MeOH})_2$ were obtained following a slightly modified protocol from the literature.⁵ In several ½ dram vials, 5 mg $\text{UO}_2(\text{NO}_3) \cdot 6 \text{H}_2\text{O}$ were combined with 4 mg benzamidoxime in 500 μL MeOH to yield dark red solutions. To each solution-containing vial were added 8 – 10 molecular sieves (4Å) which had previously been soaked in triethylamine and had not been subsequently heated or otherwise re-activated. The vials were tightly capped and allowed to sit under ambient light and temperature for 9 days, yielding discrete dark red crystals of the intended complex. The identity of the crystal was confirmed by PXRD, as shown in Figure 3.2. Several crystals were crushed with a needle in the mother liquor, consolidated into a sphere with paratone oil, and fixed to the tip of a Mite-gen crystal holder for analysis. Peak positions and intensities closely match those of the simulated PXRD.

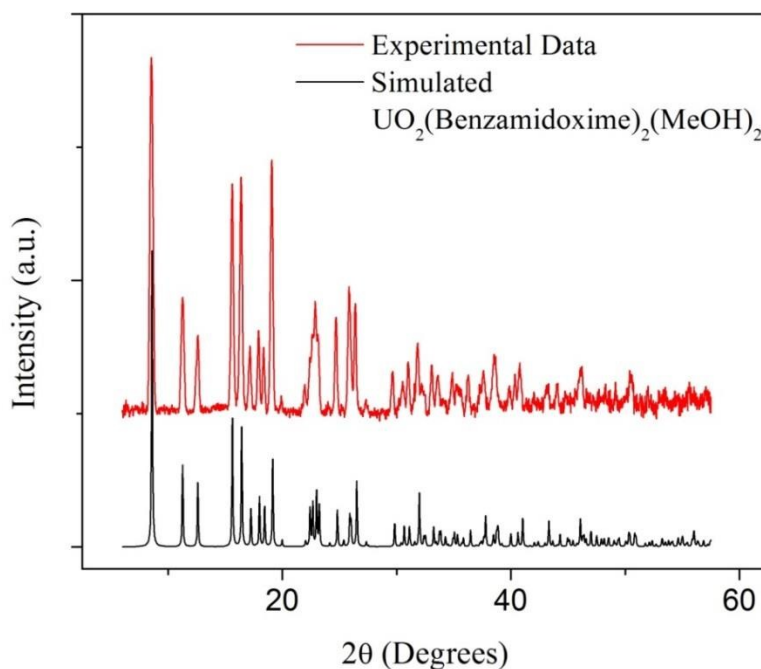


Figure S1. PXRD of $\text{UO}_2(\text{Benzamidoximate})_2(\text{MeOH})_2$ compared against the simulated PXRD spectrum.

1.2.4 Preparation of Uranyl Glutarimidedioxime Crystals Small single crystals and polycrystalline material of $\text{UO}_2(\text{Glutarimidedioximate})_2$ were prepared by a slightly modified literature protocol.⁷ In several ½ dram vials, 2 mg $\text{UO}_2(\text{NO}_3) \cdot 6 \text{H}_2\text{O}$ were combined with 1.144 mg glutarimidedioxime in 920 μL DI water with 80 μL 0.1M aqueous NaOH. The vials were tightly capped and allowed to sit under ambient light and temperature for 7 days, yielding tan polycrystalline powder of the desired complex. The identity of the crystal was confirmed by PXRD, as shown in Figure 3.3. Crystals were collected by centrifugation, suspended in EtOH and drop-cast onto a crystalline Si wafer. Due to formation of polycrystalline material, no grinding was necessary to obtain a uniform thin film. Peak positions and intensities closely match those of the simulated PXRD.

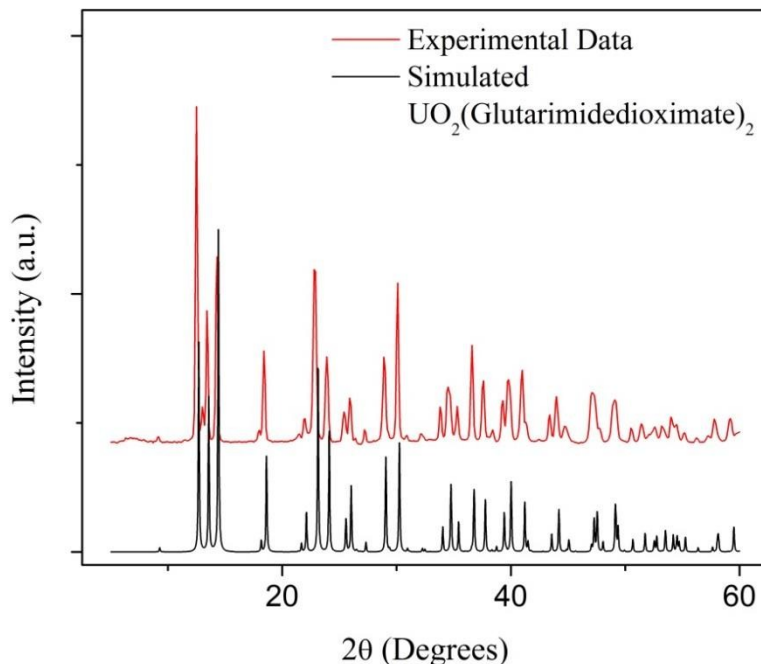


Figure S2. PXRD of $\text{UO}_2(\text{Glutarimidedioximate})_2$ compared against the simulated PXRD spectrum.

1.3 Preparation of Polymer Fibres

1.3.1 KOH Pre-treatment of Amidoxime-Functionalized Polymer Fibres Treatment of amidoxime-functionalized polymer sorbents with KOH solution prior to deployment is known to dramatically improve uranyl sorption.⁸⁻¹² Pre-treatment of the pristine amidoxime-functionalized fibres

were performed by the same protocol used to pre-treat fibres prior to seawater testing at PNNL.⁴ 25 mg (dry weight) fibres were soaked in 25 mL of an aqueous 2.5% KOH solution at 80 °C for 1 hr. The fibres were collected by gravity filtration; to preserve the fibre hydrogel, vacuum was not pulled on the fibres at any point. Fibres were washed extensively with DI water until their pH returned to 7-8. Fibres were stored in DI water at pH 7-8 until use.

1.3.2 Sorption of Uranium by KOH-Treated Fibres in Seawater Simulant Following KOH treatment, batches of fibres were used to extract uranium from seawater simulant solution, the composition of which is provided in Table 1.^{3, 4} To minimize the necessary contact time, uranium is added at a concentration of 8 ppm rather than the environmental concentration of 3.3 ppb. Vanadium is one of the major competing ions for uranium extraction from seawater, and is known to significantly decrease the sorption efficiency for amidoxime-functionalized polymer fibres. To investigate whether the presence of vanadium affects the binding motif of uranium, one batch of seawater simulant was prepared with only uranium, while the other batch also contained 5.3 ppm vanadium from the addition of sodium orthovanadate. No other competing metal ions were added to the seawater simulant solutions.

KOH-treated amidoxime-functionalized polymer fibres (25 mg dry weight, prior to KOH treatment) were suspended at a phase ratio of 25 mg L⁻¹ in the two seawater simulant solutions and agitated at 200 RPM on a plate shaker for 24 hrs contact time. Fibres were collected by filtration, washed with DI water, and dried for 24 hrs under vacuum. Uptake of uranium and vanadium was determined by ICP-MS analysis of the stock solutions and supernatant after sorption.

Table S1 Composition of Seawater Simulant^{3,4}

Chemical	Mass (L ⁻¹)
UO ₂ (NO ₃) ₂ • 6 H ₂ O	17 mg
Na ₃ VO ₄	19 mg
NaCl	25.6 g
NaHCO ₃	194 mg

1.3.3 Treatment of Environmental Seawater-Contacted Fibres Amidoxime-functionalized polymer fibres were contacted with filtered environmental seawater from Sequim Bay in flow-through experiments performed at PNNL, as published previously.⁴ In short, fibres were pre-treated with KOH as discussed above, rinsed with DI water, and packed in flow-through columns for exposure to seawater. After 42 days contact time, the samples were rinsed with DI water to remove salts and stored in DI water until sample preparation.

Seawater is known to contain significant quantities of ions capable of competing with uranium for binding sites. Table 2 displays the concentration of metals in the environmental seawater, as well as previously reported amounts adsorbed by polymer fibres of similar formulation.⁴ One environmental fibre sample was prepared for XAFS analysis “as received,” while a second fibre sample was stripped of all elements other than uranium and vanadium, as reported in the literature.¹³ To perform the elution process, 2 g fibres (wet-mass, as received) were washed with DI water and collected by gravity filtration. They were subsequently immersed in 22.5 mL of an aqueous 0.05 M HCl solution containing 1.125 g (5% w/v) L-ascorbic acid and heated overnight at 30 °C. The fibres were collected by gravity filtration and washed with DI water. They were then immersed in 22.5 mL aqueous 0.05 M HCl solution containing 240 mg (1% w/v) thiourea, heated at 30 °C for 2.5 hrs, collected by gravity filtration and washed with DI water. Both batches of polymer fibres, as received and post-elution, were first dried on a Buchner funnel, then dried under vacuum for 24 hrs. Each batch yielded ca. 65 mg dry fibres.

Dry seawater-exposed fibre samples were digested and analyzed by ICP-MS to determine the quantity of uranium, vanadium, and other metals on the fibres. 10.4 mg (dry weight) fibres as received and 11.6 mg fibres post-elution were digested as discussed in the literature.⁴ Fibres were immersed in 4 mL of a 3:1 TraceMetal Grade HCl:HNO₃ solution and agitated at 300 RPM on a plate shaker for 24 hrs. The fibres which had been eluted with 0.05 M HCl did not dissolve completely and an additional 4 mL acid were added followed by subsequent 24 hrs agitation. Samples were diluted with 18 MΩ DI water, filtered through an 0.2 µm PES syringe filter, and analyzed by ICP-MS as discussed in Section 1.1.

Table S2 Concentration of Metals in Field Test Seawater and as Adsorbed by Polymer Fibres

Element	Filtered Seawater (ng/kg)	Metal on Amidoxime Fibre (mg Metal / g Fibre)				
		Lit.	Simulant (no V) ^a	Simulant (with V) ^a	Seawater (As Received)	Seawater (Post-Elution)
V	1480	5.7	> 0.1	107 ± 5	5.8 ± 0.3	3.1 ± 0.2
U	2840	2.7	165 ± 8	62 ± 3	3.1 ± 0.2	2.9 ± 0.2
Fe	2200	1.9	---	---	0.8 ± 0.1	0.2 ± 0.1
Cu	540	1.3	---	---	0.7 ± 0.1	0.6 ± 0.1
Ni	560	0.7	---	---	0.4 ± 0.1	0.1 ± 0.1
Zn	2100	0.7	---	---	0.9 ± 0.1	< 0.1
Sr	---	0.3	---	---	0.1 ± 0.1	< 0.1
Cr	180	0.2	---	---	< 0.1	< 0.1
Mn	1200	0.1	---	---	< 0.1	< 0.1
Pb	2.5	0.1	---	---	< 0.1	< 0.1

^a. ICP-MS analysis was not performed for metals other than U and V for samples exposed to seawater simulant.

For all ICP-MS measurements, uncertainties were estimated at ±5% of the measured value.

2. Low-Energy Spectroscopy

2.1 Raman Spectroscopy

Raman spectra were collected for seawater-contacted fibres as well as both batches of simulant-contacted fibres (U only), pristine fibres, and both small molecule standards. Fibres contacted in simulant with both U and V were not analyzable, due to excessive fluorescence from bound V. Data are displayed in **Figure S3**. While features attributable to uranyl can be identified in small molecule standards and simulant-contacted fibres, the concentration of uranium on seawater-contacted fibres is insufficient for meaningful interpretation of the resulting Raman spectra.

2.2 ATR-FTIR Spectra

ATR-IR spectra were collected for seawater-contacted fibres as well as both batches of simulant-contacted fibres (U only), and pristine fibres. Data are displayed in **Figure S4**. Features attributable to uranyl cannot be positively identified in even simulant-contacted fibres, indicating the concentration of uranium on seawater-contacted fibres is insufficient for meaningful interpretation of the resulting ATR-IR spectra.

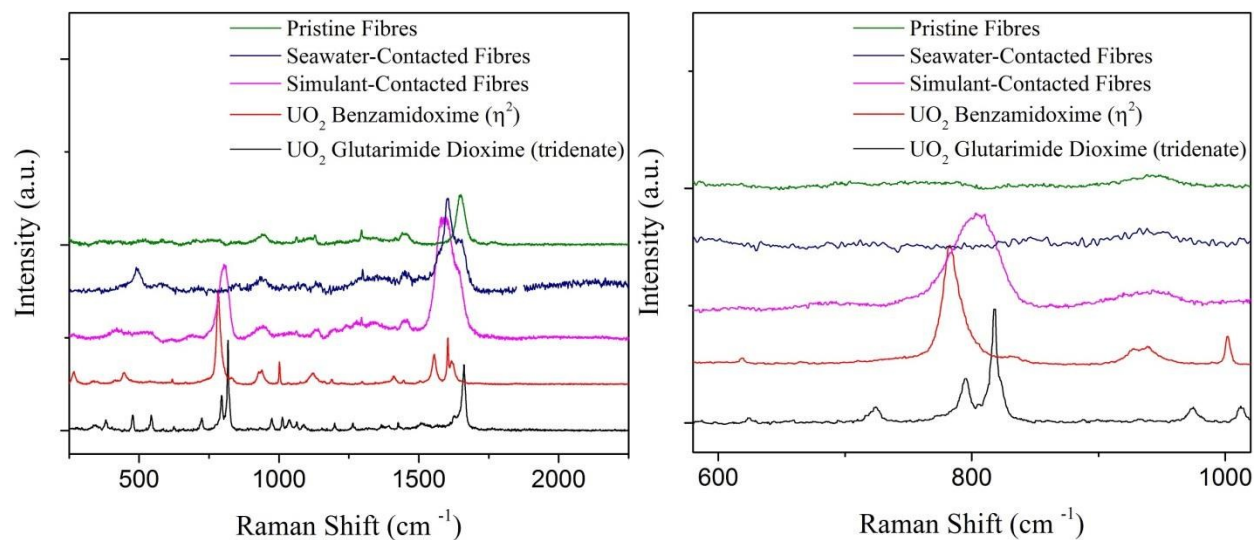


Figure S3 Raman spectra for fibre samples and small molecule standards. (Left) Raman spectra displayed from 250 – 2500 cm^{-1} . (Right) Raman spectra displayed in the region of the strong U-O_{yl} stretching frequency ($\sim 800 \text{ cm}^{-1}$). Note that no stretching frequency can be observed for the seawater-contacted fibres, revealing the limitations of this form of spectroscopy.

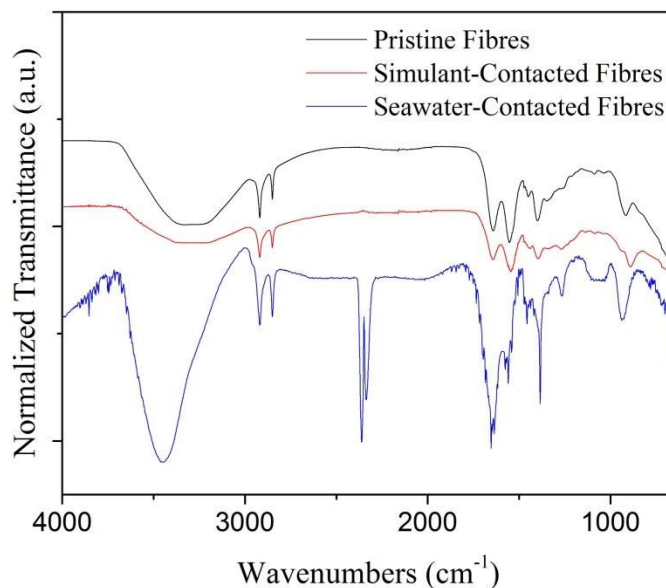


Figure S4 ATR-IR spectra for pristine fibres, simulant-contacted fibres (U only), and seawater-contacted fibres. No definitive structural information can be obtained from these spectra. The band at approximately 2350 cm^{-1} in the spectra of the seawater-contacted fibers is atmospheric CO_2 .

3. X-ray Absorption Fine Structure Spectroscopy

3.1 Preparation of XAFS Standards

The mass of uranium needed to achieve a 1 – 2.5 absorption length edge step was calculated for each small molecule standard based on the elemental composition and mass absorption coefficient for each element.¹⁴ Small molecule standards were dried under vacuum for 1 hr, ground with an agate mortar and pestle, and blended with D-(+)-Glucose to the appropriate concentration.

For each XAFS sample, approximately 35 mg dry fibres were pulverized using a Retsch CryoMill cryogenic ball mill. Samples were ground in a stainless steel 25 mL grinding jar using 15 mm stainless steel balls. The samples were pre-cooled to cryogenic temperatures for 5 minutes while milling at a rate of 5 hz, then fully pulverized for 5 minutes at 30 hz. An average particle size of 10 μm was obtained by this process. Due to the high concentration of uranium on the simulant-contacted fibres, pulverized fibres were diluted with D-(+)-Glucose to mitigate self-absorption effects.

Approximately 20 – 25 mg of sample (after diluting) was enclosed within a nylon washer of 4.953 mm inner diameter (area of 0.193 cm^2), sealed on one side with Kapton film held in place with Kapton tape. The sample was pressed thoroughly by hand to form a firm, uniform pellet, then sealed on the open side with a second piece of Kapton film secured with Kapton tape. The entire sample was placed into a baggie formed of Kapton tape which had been folded in half to prevent any contact with the adhesive. Small pieces of Kapton tape were used to seal the three open edges of the Kapton baggie. This method was approved in advance by the APS Radiation Safety Review Board for achieving the double containment necessary for analysis of radioactive samples.

3.2 Data Collection

The X-ray absorption data were collected at Beamline 10BM-B at the Advanced Photon Source (APS) at Argonne National Laboratory. Spectra were collected at the uranium L_3 -edge (17166 eV). Data for small molecule crystal standards were collected in transmission mode, while data for uranium-exposed

amidoxime-functionalized polymer fibres were collected by a Hitachi Vortex-ME4 four-element silicon drift fluorescence detector. The X-ray white beam was monochromatized by a Si(111) monochromator and detuned by 50% to reduce the contribution of higher-order harmonics to below the level of noise. The K-edge of an yttrium foil (17038 eV) was used as the reference for energy calibration and measured simultaneously for all samples. The incident beam intensity (I_0), transmitted beam intensity (I_t), and reference (I_r) were all measured by 20 cm ionization chambers with gas compositions of 80% N₂ and 20% Ar, 95% Ar and 5% N₂, and 100% N₂, respectively. All spectra were collected at room temperature.

Samples were centered on the beam and adjusted to find the most homogeneous location in the sample for data collection. The beam was reduced to dimensions of 400 × 3100 μm for all data collection. Data were collected over six regions: -250 to -30 eV (10 eV step size, dwell time of 0.25 seconds), -30 to -5 eV (5 eV step size, dwell time of 0.5 seconds), -5 to 30 eV (1 eV step size), 3 Å⁻¹ to 6 Å⁻¹ (0.05 Å⁻¹ step size, dwell time of 2 seconds), 6 Å⁻¹ to 9 Å⁻¹ (0.05 Å⁻¹ step size, dwell time of 4 seconds), and 9 Å⁻¹ to 15 Å⁻¹ (0.05 Å⁻¹ step size, dwell time of 8 seconds). Three scans were collected at room temperature (~25°C) for each sample.

The data were processed and analyzed using the Athena and Artemis programs of the IFEFFIT package based on FEFF 6.^{15, 16} Reference foil data were aligned to the first zero-crossing of the second derivative of the normalized $\mu(E)$ data, which was subsequently calibrated to the literature E_0 for the yttrium K-edge (17038 eV). Spectra were averaged in $\mu(E)$ prior to normalization. The background was removed and the data were assigned an Rbkg value of 0.8, slightly less than one-half the value of the half-path length for the nearest scattering element, prior to normalizing to obtain a unit edge step.

All data were initially fit with k-weighting of 1, 2, and 3, then finalized with k³-weighting in R-space. Structural parameters that were determined by the fits include the degeneracy of the scattering path (N_{degen}), the change in R_{eff} (ΔR_i), the relative mean square displacement of the scattering element (σ_i^2), the passive electron reduction factor (S_0^2), and the energy shift of the photoelectron, (ΔE_0). S_0^2 was found to converge to 1.0 ± 0.10 for all fits (standards and polymer fibres) and was thus fixed at that value for all models. Two different ΔE values were used, one for the tightly-bound axial oxygen and the second

for all other scattering paths.^{17, 18} For each fit, the fit range (ΔR), data range (Δk), number of independent points (N_{idp}), number of variables (N_{var}), degree of freedom (ν), reduced chi-squared value (χ_{ν}^2), and R-factor (R) are in Table S3. For each fit, the number of independent points was not permitted to exceed 2/3 the number of variables, in keeping with the Nyquist criterion.^{18, 19}

Table S3 Data range and goodness-of-fit parameters for best-fit models

Sample	ΔR (Å)	Δk (Å ⁻¹)	N_{idp}	N_{var}	ν	χ_{ν}^2	R (%)
UO ₂ (Benzamidoxime) ₂	1 – 4.0	2.5 – 14.0	21	12	9	84.0	1.2
UO ₂ (Glutarimidodioxime) ₂	1 – 4.0	2.3 – 14.0	22	14	8	132	2.0
Fibres in Simulant (U only)	1 – 3.5	2.3 – 14.0	18	11	7	11.6	1.4
Fibres in Simulant (U and V)	1 – 3.5	2.6 – 13.9	17	11	6	2.7	1.3
Fibres from Seawater (as received)	1 – 3.5	2.0 – 14.0	19	12	6	6.0	1.8
Fibres from Seawater (post-elution)	1 – 3.5	2.3 – 12.7	16	10	6	4.5	3.5

4. XANES Analysis and Linear Combination Fitting

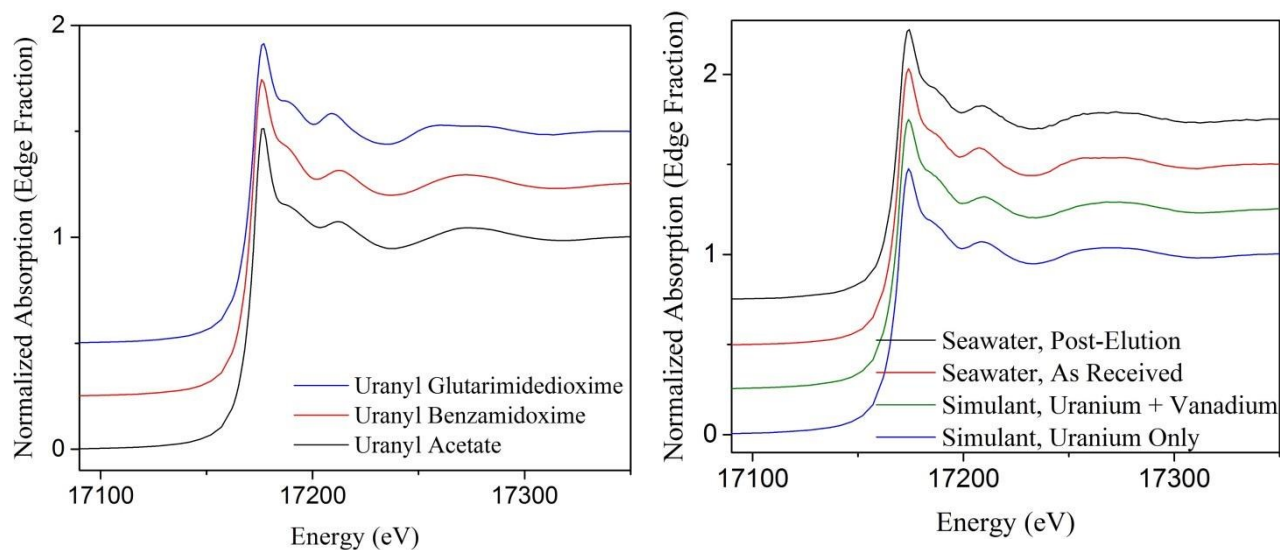


Figure S5 XANES region of small molecule standards and uranyl acetate dehydrate (left) and uranyl-exposed polymer fibre samples (right) measured at the uranium L₃-edge. Normalized absorption spectra are offset by an edge fraction of 0.25 for the sake of clarity.

The absence of any pre-edge feature, a common oxidation state, and similar coordination environment for all samples result in a XANES region with few substantial differences between small molecule standards or polymer-bound uranium samples. It is known the first feature in the XANES region, at approximately 17225 eV, can be attributed to direct scattering off the axial oxygen of uranyl. The second feature, beginning at approximately 17250 eV, is due to the equatorially-coordinated atoms.²⁰ It is possible to observe a slight difference in the second feature between the uranyl glutarimidedioxime standard, as compared with uranyl benzamidoxime or uranyl acetate. However, these subtle differences are insufficient for deconvoluting the binding environments on the polymer fibres.

XANES is useful in determining the average oxidation state of the absorbing element, as the position of the edge is related to the valence state. There is no precedent to suggest that uranyl is reduced in seawater to influence the binding environment. Previous work reveals the edge position for U(VI) and U(IV) standards differ by more than 4 eV.¹⁸ Our data were aligned to a Y reference foil for which data were collected simultaneously with data collection for our samples of interest. We estimate the uncertainty in the uranium oxidation state in our small molecule standards to be $\pm 5\%$, and qualitative comparison between all samples reveal no appreciable difference in edge position. No significant reduction of U(VI) to U(IV) or mineralization as metallic U(0) is observed. This observation is entirely expected and consistent with volumes of literature.

Linear combination fitting was attempted for all non-eluted adsorbent samples using XANES region spectra from small molecule complexes $\text{UO}_2(\text{Benzamidoximate})_2(\text{MeOH})_2$ and $\text{UO}_2(\text{Glutarimide Dioxime})_2$ as standards. In all instances, the best fit was achieved using only spectral contributions from the $\text{UO}_2(\text{Benzamidoximate})_2(\text{MeOH})_2$ standard. However, in all instances a relatively large residual remained following the linear combination fit, with the most significant occurring for the seawater-contacted fibres. The tightly-bound axial oxygen and similar equatorial coordination environment results in the similarity for fits of fibres exposed to seawater simulant. As mentioned previously, the lack of unique characteristic features hinders much of the utility of XANES analysis, but the relatively large amount of residual in all linear combination fits suggests the fibre-bound uranium atomic environment is

not represented well using just the small molecule standards. These negative results support our assertion that uranyl is bound by a motif that differs from those predicted computationally or from small molecule studies.

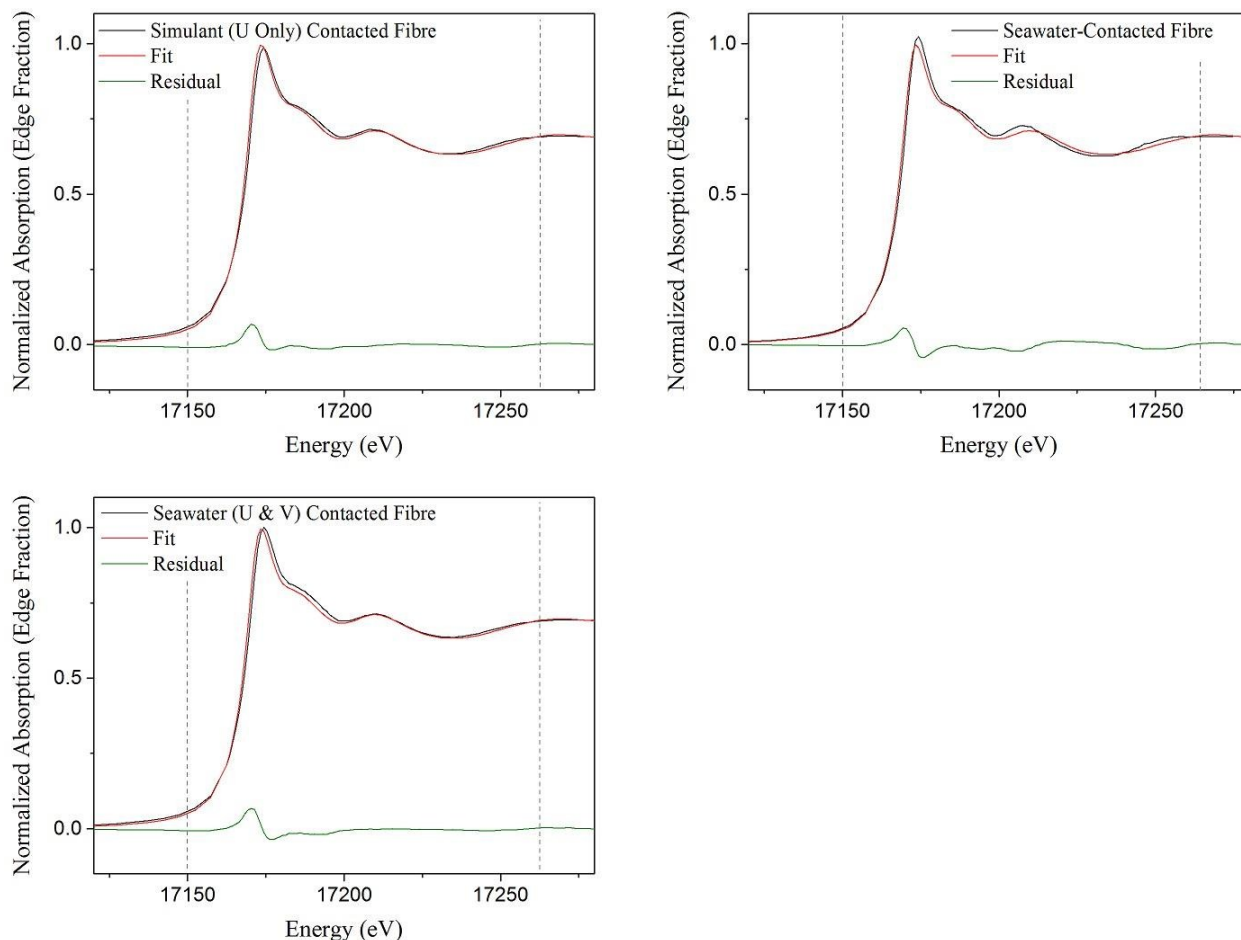


Figure S6 Linear Combination Fits for (top left) simulant-contacted (U only) polymer fibres, (top right) seawater-contacted polymer fibres, and (bottom left) simulant-contacted (U & V) polymer fibres. XANES data are plotted in black, the best fit is plotted in red, and the residual difference is plotted in green. Despite using both small molecule standards as components in the fit, all best fitted models only used spectral contributions from $\text{UO}_2(\text{Benzamidoximate})_2(\text{MeOH})_2$. The large residual suggests this model is a reasonable approximation, but cannot fully resolve all spectral features for the experimental XANES data.

5. EXAFS Fitting

5.1 Small Molecule Standards.

5.1.1 Uranyl Benzamidoxime. All scattering paths used and parameters determined in the fit of $\text{UO}_2(\text{Benzamidoxime})_2 \cdot 2 \text{ MeOH}$ are displayed in Table S6. The structure model was based on the obtained single crystal structure of $\text{UO}_2(\text{Benzamidoxime})_2 \cdot 2 \text{ MeOH}$. (Aside: This single crystal structure was previously reported.⁵ The only difference between the single crystal reported herein and the previously reported crystal structure is the temperature at which the structures were obtained. Data was collected at 100K, while data for the previously-reported crystal was collected at 173 K). The best-fit model contains two axial oxygen on uranyl (O_{y1}) and direct scattering paths from first shell oxygen (O) and nitrogen (N), and second shell carbon (C). Multiple scattering paths from the axial oxygen contributed to the fits significantly, which can be attributed to strong uranyl binding as well as the linear orientation of $\text{O}_{y1}\text{-U-O}_{y1}$. Other multiple scattering paths included four double scattering paths between the amidoxime oxygen and nitrogen, and two obtuse triangular paths between the amidoxime nitrogen and carbon. The degeneracy of O_{y1} was fixed at two, while the coordination number of O, N, and C were allowed to vary. Change in scattering half-path length (ΔR) and mean squared relative deviation (σ^2) were free parameters for all direct scattering paths. ΔR and σ^2 for O_{y1} was refined simultaneously for both uranyl benzamidoxime and uranyl glutarimidedioxime standards. Errors for multiple scattering pathways were obtained by standard propagation of error from their constituent single scattering pathways.

Table S4. Paths, Initial Path Lengths, Initial Degeneracy and Parameters for Fitting Uranyl Benzamidoxime

Scattering Path	N_{degen}	$R(\text{\AA})$	$\Delta R(\text{\AA})$	$\sigma^2(\text{\AA}^2)$	ΔE
$U \rightarrow O_{yl}$	2	1.80	$\Delta R-O_{yl}$	σ^2-O_{yl}	ΔE_1
$U \rightarrow O$	4	2.35	$\Delta R-O$	σ^2-O	ΔE_2
$U \rightarrow N$	2	2.44	$\Delta R-N$	σ^2-N	ΔE_2
$U \rightarrow C$	4	3.57	$\Delta R-C$	σ^2-C	ΔE_2
$U \rightarrow O_{yl(1)} \rightarrow O_{yl(2)}$	2	3.59	$2 \times \Delta R-O_{yl}$	$2 \times \sigma^2-O_{yl}$	ΔE_1
$U \rightarrow O_{yl(1)} \rightarrow U \rightarrow O_{yl(2)}$	2	3.59	$2 \times \Delta R-O_{yl}$	$2 \times \sigma^2-O_{yl}$	ΔE_1
$U \rightarrow O_{yl(1)} \rightarrow U \rightarrow O_{yl(1)}$	2	3.59	$2 \times \Delta R-O_{yl}$	$2 \times \sigma^2-O_{yl}$	ΔE_1
$U \rightarrow N \rightarrow C$	2	3.65	$0.5 \times \Delta R-N$ $+ 0.5 \times \Delta R-C$	$0.5 \times \sigma^2-N$ $+ 0.5 \times \sigma^2-C$	ΔE_2

Table S5 Best-Fit Values for Uranyl Benzamidoxime Small Molecule Standard

Scattering Path	N_{degen}	$R(\text{\AA})$	error	$\sigma^2(\text{\AA}^2)$	error
$U \rightarrow O_{yl}$	2 ^a	1.81	0.01	0.002	< 0.001
$U \rightarrow O$	4 ± 1	2.36	0.02	0.005	0.002
$U \rightarrow N$	2 ± 0.2 ^b	2.51	0.03	0.004	0.002
$U \rightarrow C$	3 ± 2	3.48	0.05	0.003	0.002
$U \rightarrow O_{yl(1)} \rightarrow O_{yl(2)}$	2 ^a	3.62	0.01	0.005	0.001
$U \rightarrow O_{yl(1)} \rightarrow U \rightarrow O_{yl(2)}$	2 ^a	3.62	0.01	0.005	0.001
$U \rightarrow O_{yl(1)} \rightarrow U \rightarrow O_{yl(1)}$	2 ^a	3.62	0.01	0.005	0.001
$U \rightarrow N \rightarrow C$	2 ± 0	3.64	0.03	0.003	0.001
$\Delta E_1 = 2 \pm 2 \text{ eV}$					
$\Delta E_2 = 1 \pm 2 \text{ eV}$					

^a The coordination number for $U \rightarrow O_{yl}$ was held at 2 for the model.

^b The uncertainty in step height during normalization can be as large as 10%. As S_0^2 , N , and step height are all components of the amplitude, the coordination number cannot be determined to greater accuracy than 10%.¹⁸

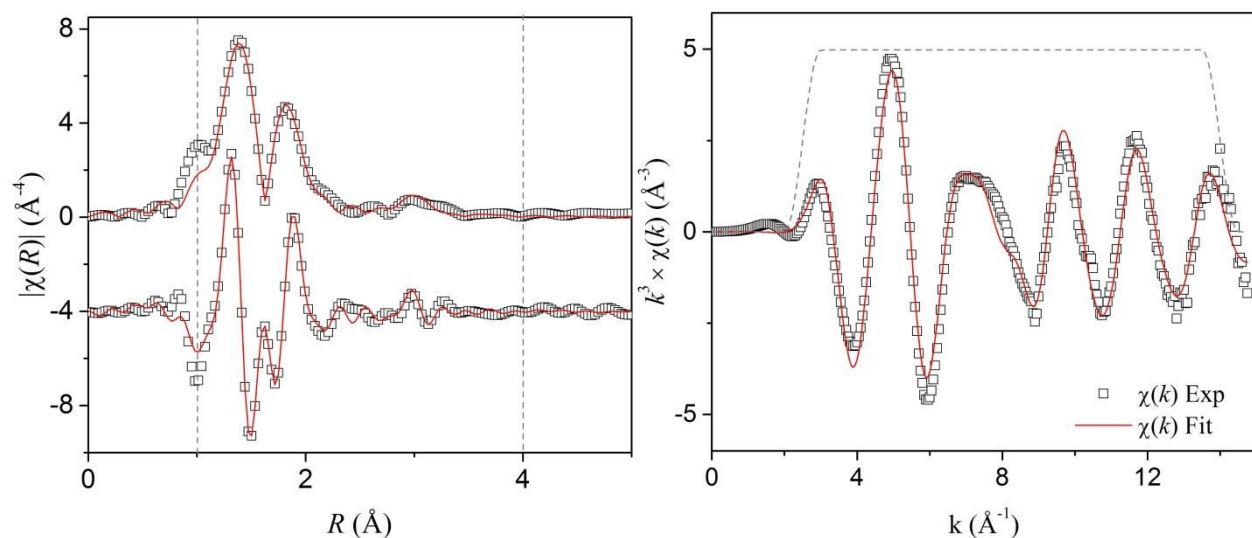


Figure S7 Data (open symbols) and best-fit model (line) for fit of EXAFS data for uranyl benzamidoxime small molecule standard. The Fourier transform is displayed on the left, with the magnitude (top) and real components. The right column is plotted in k -space. All plots are displayed with k^3 -weighting. Grey lines display the fitting window.

5.1.2 Uranyl Glutarimidedioxime. All scattering paths and parameters determined in the fit of $\text{UO}_2(\text{Glutarimidedioxime})_2$ are displayed in Table S6. As with uranyl benzamidoxime, strong contributions were required from both direct and multiple scattering off the axial oxygen. Direct scattering paths were from each of the oxime oxygen ($\text{O}_{\text{ox}1}$, $\text{O}_{\text{ox}2}$) and nitrogen (N_{ox}), the imide nitrogen (N_{im}), and the oxime carbon (C). Multiple scattering paths included four obtuse triangular paths between the oxime oxygen and nitrogen, and four obtuse triangular paths between the imide nitrogen and carbon. As with uranyl benzamidoxime, the degeneracy of $\text{O}_{\text{y}1}$ was fixed at two, while the coordination number of O_{ox} and N_{im} , were allowed to vary. The degeneracy of $\text{O}_{\text{ox}1}$ and $\text{O}_{\text{ox}2}$ were each equal to $0.5 \times$ the variable O_{ox} , and the coordination number of N_{ox} and C were defined as $2 \times \text{N}_{\text{im}}$. Change in scattering half-path length (ΔR) and mean squared relative deviation (σ^2) were free parameters for all direct scattering paths, and ΔR and σ^2 for $\text{O}_{\text{y}1}$ was refined simultaneously for both uranyl benzamidoxime and uranyl glutarimidedioxime standards. The final evaluated parameters for all scattering paths for both standards

are provided in Table 3.7. Errors for multiple scattering pathways were obtained by standard propagation of error from their constituent single scattering pathways.

Table S6 Paths, Initial Path Lengths, Initial Degeneracies and Parameters for Fitting Uranyl Glutarimidedioxime

Scattering Path	N_{degen}	$R(\text{\AA})$	$\Delta R(\text{\AA})$	$\sigma^2(\text{\AA}^2)$	ΔE
$U \rightarrow O_{\text{yl}}$	2	1.79	$\Delta R-O_{\text{yl}}$	σ^2-O_{yl}	ΔE_1
$U \rightarrow O_{\text{ox1}}$	2	2.43	$\Delta R-O$	σ^2-O	ΔE_2
$U \rightarrow O_{\text{ox2}}$	2	2.53	$\Delta R-O$	σ^2-O	ΔE_2
$U \rightarrow N_{\text{im}}$	2	2.56	$\Delta R-N_{\text{im}}$	σ^2-N	ΔE_2
$U \rightarrow N_{\text{ox}}$	4	3.36	$\Delta R-N_{\text{ox}}$	σ^2-N	ΔE_2
$U \rightarrow C$	4	3.47	$\Delta R-C$	σ^2-C	ΔE_2
$U \rightarrow O_{\text{yl}(1)} \rightarrow O_{\text{yl}(2)}$	2	3.57	$2 \times \Delta R-O_{\text{yl}}$	$2 \times \sigma^2-O_{\text{yl}}$	ΔE_1
$U \rightarrow O_{\text{yl}(1)} \rightarrow U \rightarrow O_{\text{yl}(2)}$	2	3.57	$2 \times \Delta R-O_{\text{yl}}$	$2 \times \sigma^2-O_{\text{yl}}$	ΔE_1
$U \rightarrow O_{\text{yl}(1)} \rightarrow U \rightarrow O_{\text{yl}(1)}$	2	3.57	$2 \times \Delta R-O_{\text{yl}}$	$2 \times \sigma^2-O_{\text{yl}}$	ΔE_1
$U \rightarrow O_{\text{ox}} \rightarrow N_{\text{ox}}$	4	3.57	$0.25 \times \Delta R-O_{\text{ox1}}$ $+ 0.25 \times \Delta R-O_{\text{ox2}}$ $+ 0.5 \times \Delta R-N_{\text{ox}}$	$0.5 \times \sigma^2-O$ $+ 0.5 \times \sigma^2-N$	ΔE_2
$U \rightarrow N_{\text{ox}} \rightarrow C$	4	3.70	$0.5 \times \Delta R-N_{\text{ox}}$ $+ 0.5 \times \Delta R-C$	$0.5 \times \sigma^2-N$ $+ 0.5 \times \sigma^2-C$	ΔE_2

Table S7 Best-Fit Values for Uranyl Glutarimidedioxime Small Molecule Standard

Scattering Path	N_{degen}	$R(\text{\AA})$	error	$\sigma^2(\text{\AA}^2)$	error
$U \rightarrow O_{\text{yl}}$	2 ^a	1.80	0.01	0.002	< 0.001
$U \rightarrow O_{\text{ox1}}$	1.5 ± 1	2.42	0.02	0.005	0.003
$U \rightarrow O_{\text{ox2}}$	1.5 ± 1	2.54	0.02	0.005	0.003
$U \rightarrow N_{\text{im}}$	1.5 ± 1	2.56	0.02	0.003	0.001
$U \rightarrow N_{\text{ox}}$	3 ± 2	3.36	0.03	0.003	0.001
$U \rightarrow C$	3 ± 2	3.47	0.01	0.004	0.002
$U \rightarrow O_{\text{yl}(1)} \rightarrow O_{\text{yl}(2)}$	2 ^a	3.60	0.01	0.006	0.001
$U \rightarrow O_{\text{yl}(1)} \rightarrow U \rightarrow O_{\text{yl}(2)}$	2 ^a	3.60	0.01	0.006	0.001
$U \rightarrow O_{\text{yl}(1)} \rightarrow U \rightarrow O_{\text{yl}(1)}$	2 ^a	3.60	0.01	0.006	0.001
$U \rightarrow O_{\text{ox}} \rightarrow N_{\text{ox}}$	3 ± 2	3.59	0.02	0.004	0.002
$U \rightarrow N_{\text{ox}} \rightarrow C$	3 ± 2	3.71	0.02	0.003	0.002
$\Delta E_1 = 1 \pm 2 \text{ eV}$					
$\Delta E_2 = 2 \pm 2 \text{ eV}$					

^a The coordination number for $U \rightarrow O_{\text{yl}}$ was held at 2 for the model.

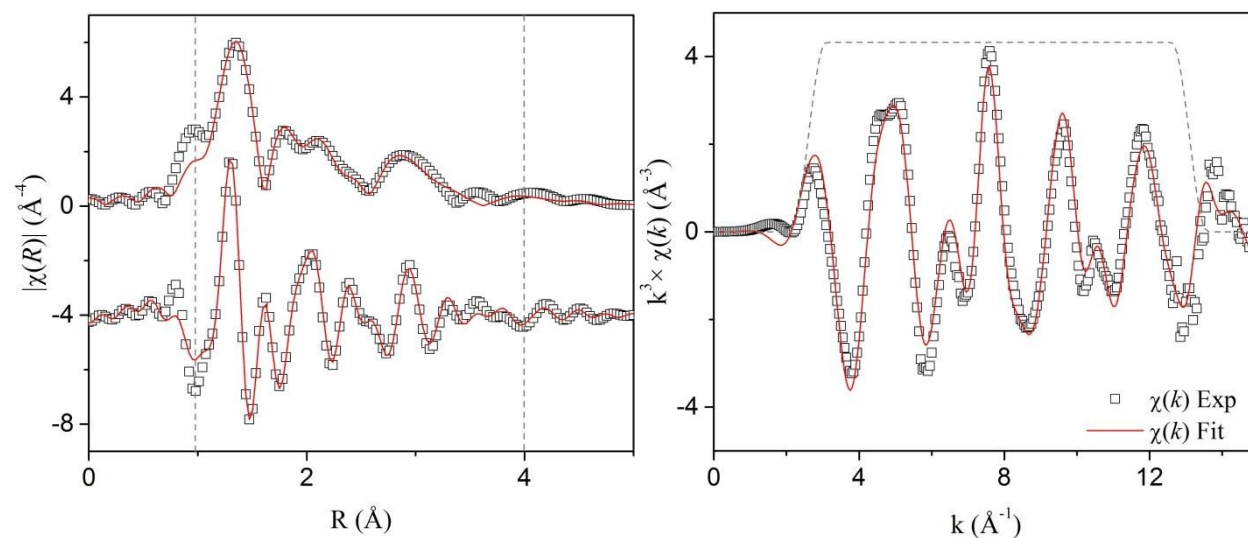


Figure S8 Data (open symbols) and best-fit model (line) for fit of EXAFS data for uranyl glutarimidedioxime small molecule standard. The Fourier transform is displayed on the left, with the magnitude (top) and real components. The right column is plotted in k -space. All plots are displayed with k^3 -weighting. Grey lines display the fitting window.

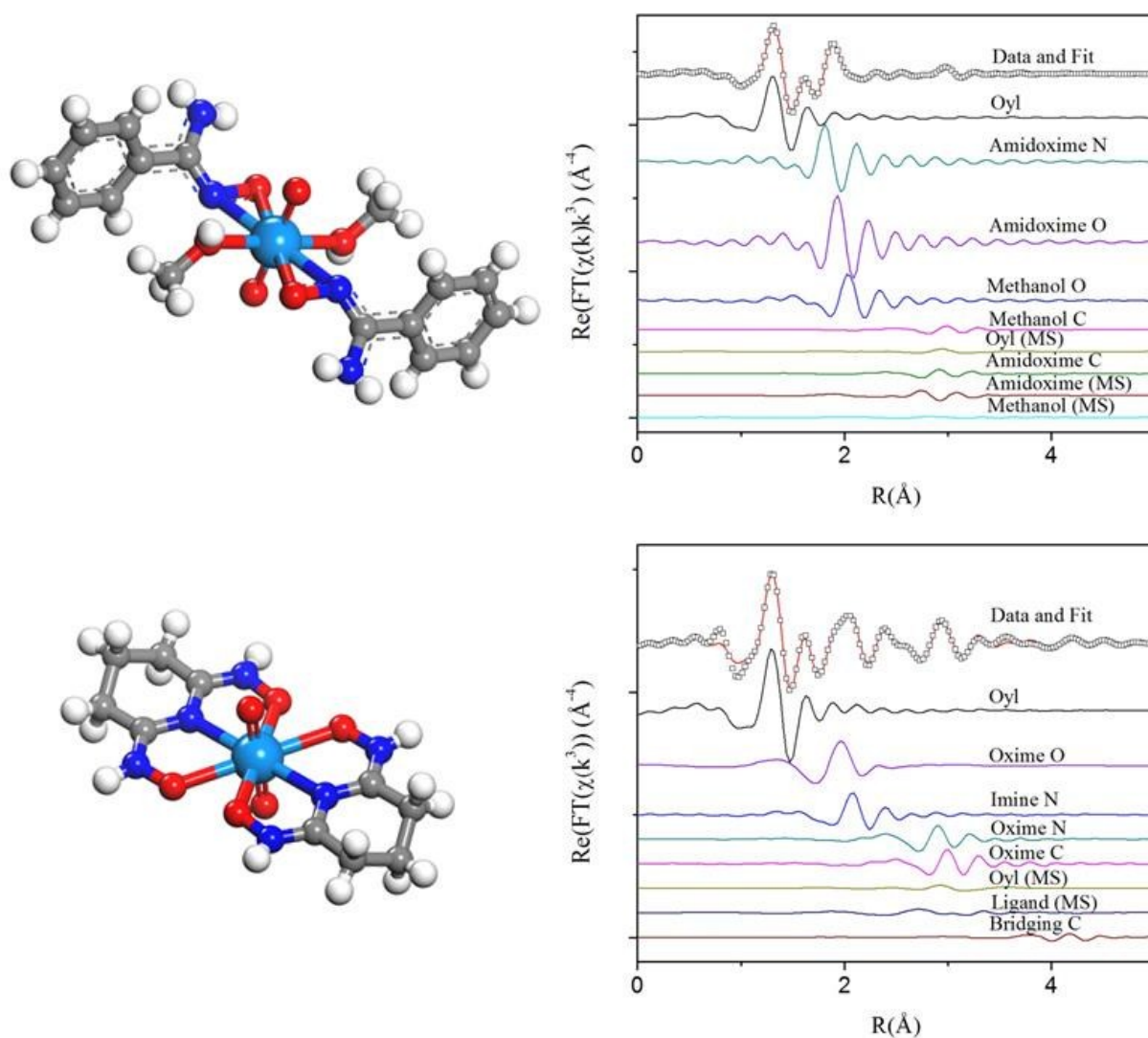


Figure S9. The real part of the Fourier transform of the uranium L_3 -edge EXAFS spectrum (open symbols) and fit (red line) for small molecule standards uranyl benzamidoxime (top) and uranyl glutarimidedioxime (bottom). Components of the fit are displayed below, with the corresponding crystal structure to the left. The crystal structure for uranyl glutarimidedioxime was obtained from the literature.⁷ Multiple scattering paths are summed and displayed as one path, denoted by a label containing (MS).

5.2 Polymer Fibres

Fits of polymer fibre data were attempted in a bottom-up fashion using models representative of each of the four proposed binding configurations. While more distant scattering paths were progressively included, refined values for previously established scattering paths were used as initial guesses, but allowed to vary freely to avoid introduction of systematic error. For all models, equatorial light scatterers converged to approximately 5-6 atoms, consistent with previous XAFS and crystallographic studies. Scattering paths were added one at a time for different elements at different distances and evaluated in the real-space component of the Fourier transform. Paths which required indefensible changes in scatterer half-path length or mean squared relative deviation were discarded. Paths representative of carbonate were investigated for all polymer fibres, while paths representative of phosphates, μ_2 -oxo bridging Cu, Fe, Zn, Ni, and V, and Na, Ca, and Mg cations were considered for all seawater-contacted fibres. Iterative refinement of the fits resulted in the finalized models discussed below.

5.2.1 Simulant-Contacted Fibres (Uranium Only). The model used to fit the fibre data was composed of several shells of light scattering elements. The first shell was composed exclusively of the tightly-bound uranyl axial oxygen (O_{yl}) with degeneracy fixed at 2. The second shell was composed of light scatterers at two different distances with equal, but variable degeneracy (O_1, N_1). The third shell was composed of light scatterers at different distances with equal, but variable degeneracy (N_2, C). ΔR and σ^2 were free parameters for all direct scattering paths. Degeneracy was a free parameter for all direct scattering paths except O_{yl} . This model structure is most consistent with a coordination environment consisting of 2-3 chelating ligands per uranyl. Data were not fit beyond 3.5 Å in R-space due to the large noise in the data.

Of particular note, extensive efforts were made to fit this data using a model representative of η^2 -chelating ligands. A reasonable fit can be obtained with this model, affording an R-factor of 1.8 and a χ^2 of 16.5 over the same fitting range. In addition to being a statistically less rigorous fit than that of the chelate model, the magnitude of the fit was consistently lower than the experimental data at higher values of R.

Table S8 Paths, Initial Path Lengths, Degeneracies, and Parameters for Fitting Polymer Fibres Contacted with Seawater Simulant (Uranium Only)

Scattering Path	N_{degen}	$R(\text{\AA})$	$\Delta R(\text{\AA})$	$\sigma^2(\text{\AA}^2)$	ΔE_1
$U \rightarrow O_{yl}$	2	1.79	$\Delta R-O_{yl}$	σ^2-O_{yl}	ΔE_1
$U \rightarrow O_1$	CN_1	2.30	$\Delta R-O$	σ^2-O	ΔE_2
$U \rightarrow N_1$	CN_1	2.45	$\Delta R-O$	σ^2-O	ΔE_2
$U \rightarrow N_2$	CN_2	3.31	$\Delta R-N$	σ^2-N	ΔE_2
$U \rightarrow C$	CN_2	3.47	$\Delta R-C$	σ^2-C	ΔE_2
$U \rightarrow O_1 \rightarrow N_2$	CN_1	3.53	$0.5 \times \Delta R-O_1$ $+ 0.5 \times \Delta R-N_2$	$0.5 \times \sigma^2-O$ $+ 0.5 \times \sigma^2-N$	ΔE_2
$U \rightarrow O_{yl(1)} \rightarrow O_{yl(2)}$	2	3.57	$2 \times \Delta R-O_{yl}$	$2 \times \sigma^2-O_{yl}$	ΔE_1
$U \rightarrow O_{yl(1)} \rightarrow U \rightarrow O_{yl(2)}$	2	3.57	$2 \times \Delta R-O_{yl}$	$2 \times \sigma^2-O_{yl}$	ΔE_1
$U \rightarrow O_{yl(1)} \rightarrow U \rightarrow O_{yl(1)}$	2	3.57	$2 \times \Delta R-O_{yl}$	$2 \times \sigma^2-O_{yl}$	ΔE_1
$U \rightarrow O_{yl} \rightarrow O_1$	$2 \times \text{CN}_1$	3.70	$0.5 \times \Delta R-O_{yl}$ $+ 0.5 \times \Delta R-O_1$	$0.5 \times \sigma^2-O_{yl} +$ $0.5 \times \sigma^2-O$	ΔE_1

Table S9 Best Fit Values for Polymer Fibres Contacted with Seawater Simulant (Uranium Only)

Scattering Path	N_{degen}	$R(\text{\AA})$	error	$\sigma^2(\text{\AA}^2)$	error
$U \rightarrow O_{yl}$	2 ^a	1.80	0.01	0.002	< 0.001
$U \rightarrow O_1$	2.8 ± 0.6	2.35	0.02	0.005	0.003
$U \rightarrow N_1$	2.8 ± 0.6	2.49	0.02	0.005	0.003
$U \rightarrow N_2$	2.8 ± 1.2	3.37	0.05	0.003	0.001
$U \rightarrow C$	2.8 ± 1.2	3.48	0.03	0.004	0.002
$U \rightarrow O_1 \rightarrow N_2$	2.8 ± 0.6	3.59	0.03	0.004	0.002
$U \rightarrow O_{yl(1)} \rightarrow O_{yl(2)}$	2 ^a	3.60	0.01	0.004	0.001
$U \rightarrow O_{yl(1)} \rightarrow U \rightarrow O_{yl(2)}$	2 ^a	3.60	0.01	0.004	0.001
$U \rightarrow O_{yl(1)} \rightarrow U \rightarrow O_{yl(1)}$	2 ^a	3.60	0.01	0.004	0.001
$U \rightarrow O_{yl} \rightarrow O_1$	5.6 ± 0.4	3.59	0.01	0.003	0.002
$\Delta E_1 = 0 \pm 1 \text{ eV}$					
$\Delta E_2 = 2 \pm 2 \text{ eV}$					

^a The coordination number for $U \rightarrow O_{yl}$ was held at 2 for the model.

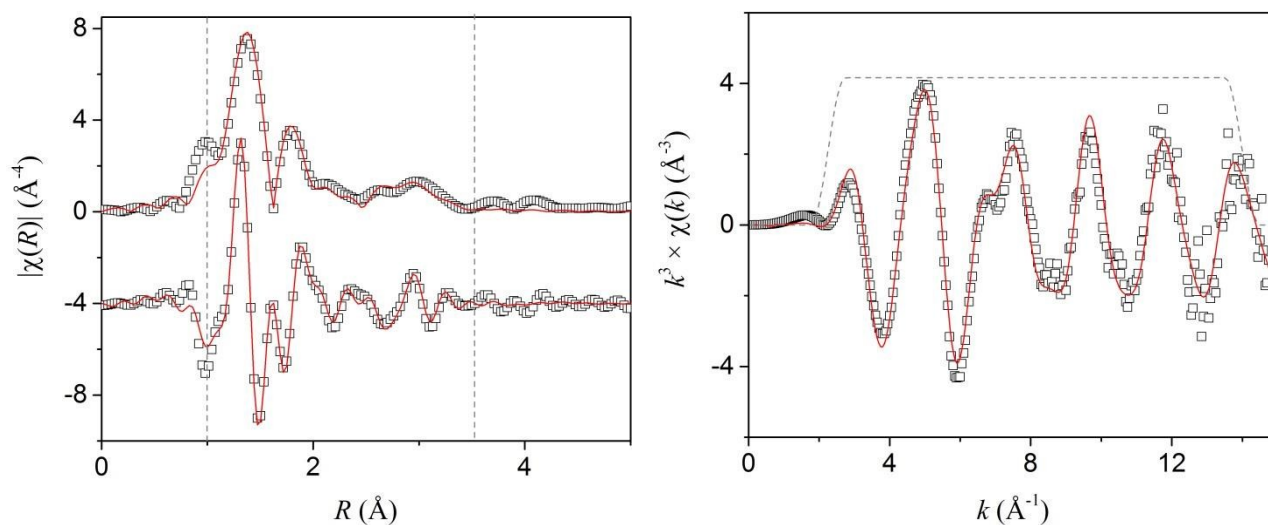


Figure S10 Data (open symbols) and best-fit chelation model (line) for fit of EXAFS data for polymer fibres contacted with seawater simulant containing uranium (only). The Fourier transform is displayed on the left, with the magnitude (top) and real components. The right column is plotted in k -space. All plots are displayed with k^3 -weighting. Grey lines display the fitting window.

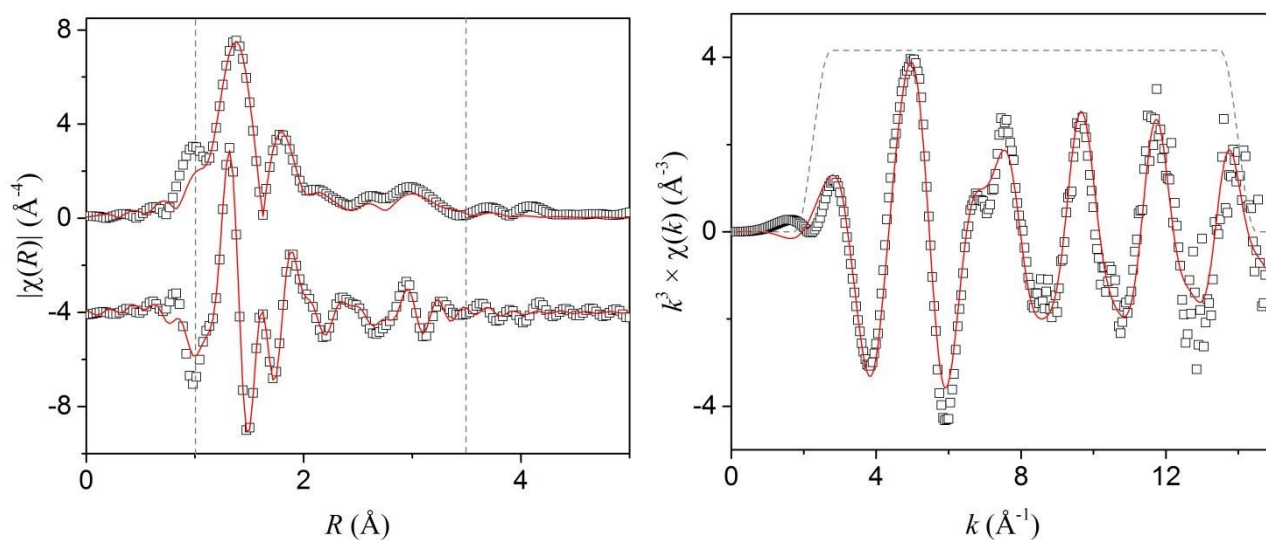


Figure S11 Data (open symbols) and fit for η^2 -model (line) for fit of EXAFS data for polymer fibres contacted with seawater simulant containing uranium (only). The Fourier transform is displayed on the left, with the magnitude (top) and real components. The right column is plotted in k -space. An R-factor

of 1.8 and a χ_v^2 of 16.5 were obtained for these fits, both of which are higher than metrics obtained for the fit using the chelator model. Also note the systemically lower intensity of the fit at approximately 2.5 - 3Å. At this distance for the η^2 -model, only the oxime carbon and multiple scattering paths are capable of contributing intensity. In contrast, there are approximately 2× the number of atoms at the same distance in the chelating model. All plots are displayed with k^3 -weighting. Grey lines display the fitting window.

5.2.2 Simulant-Contacted Fibres (Uranium and Vanadium). The model used to fit the fibre data was identical to that of simulant-contacted fibres (uranium only). The first shell was composed exclusively of the tightly-bound uranyl axial oxygen (O_{yl}) with degeneracy fixed at 2. The second shell was composed of light scatterers at two different distances with equal, but variable degeneracy (O_1, N_1). The third shell was composed of light scatterers at different distances with equal, but variable degeneracy (N_2, C). ΔR and σ^2 were free parameters for all direct scattering paths. Degeneracy was a free parameter for all direct scattering paths except O_{yl} . This model structure is most consistent with a coordination environment consisting of 2-3 chelating ligands per uranyl. Data were not fit beyond 3.5 Å in R-space due to the large noise in the data.

Table S10 Paths, Initial Path Lengths, Degeneracies, and Parameters for Fitting Polymer Fibres Contacted with Seawater Simulant (Uranium and Vanadium)

Scattering Path	N_{degen}	$R(\text{Å})$	$\Delta R(\text{Å})$	$\sigma^2(\text{Å}^2)$	ΔE_1
$U \rightarrow O_{yl}$	2	1.79	$\Delta R - O_{yl}$	$\sigma^2 - O_{yl}$	ΔE_1
$U \rightarrow O_1$	CN_1	2.30	$\Delta R - O$	$\sigma^2 - O$	ΔE_2
$U \rightarrow N_1$	CN_1	2.45	$\Delta R - O$	$\sigma^2 - O$	ΔE_2
$U \rightarrow N_2$	CN_2	3.31	$\Delta R - N$	$\sigma^2 - N$	ΔE_2
$U \rightarrow C$	CN_2	3.47	$\Delta R - C$	$\sigma^2 - C$	ΔE_2
$U \rightarrow O_1 \rightarrow N_2$	CN_2	3.53	$0.5 \times \Delta R - O_1$ $+ 0.5 \times \Delta R - N_2$	$0.5 \times \sigma^2 - O$ $+ 0.5 \times \sigma^2 - N$	ΔE_2
$U \rightarrow O_{yl(1)} \rightarrow O_{yl(2)}$	2	3.57	$2 \times \Delta R - O_{yl}$	$2 \times \sigma^2 - O_{yl}$	ΔE_1
$U \rightarrow O_{yl(1)} \rightarrow U \rightarrow O_{yl(2)}$	2	3.57	$2 \times \Delta R - O_{yl}$	$2 \times \sigma^2 - O_{yl}$	ΔE_1
$U \rightarrow O_{yl(1)} \rightarrow U \rightarrow O_{yl(1)}$	2	3.57	$2 \times \Delta R - O_{yl}$	$2 \times \sigma^2 - O_{yl}$	ΔE_1
$U \rightarrow O_{yl} \rightarrow O_1$	$2 \times \text{CN}_1$	3.70	$0.5 \times \Delta R - O_{yl}$ $+ 0.5 \times \Delta R - O_1$	$0.5 \times \sigma^2 - O_{yl} +$ $0.5 \times \sigma^2 - O$	ΔE_1

Table S11 Best Fit Values for Polymer Fibres Contacted with Seawater Simulant (Uranium and Vanadium)

Scattering Path	N_{degen}	$R(\text{\AA})$	error	$\sigma^2 (\text{\AA}^2)$	error
$U \rightarrow O_{y1}$	2 ^a	1.80	0.01	0.002	< 0.001
$U \rightarrow O_1$	3.1 ± 0.7	2.35	0.02	0.006	0.002
$U \rightarrow N_1$	3.1 ± 0.7	2.49	0.02	0.006	0.002
$U \rightarrow N_2$	3.4 ± 1.1	3.37	0.04	0.006	0.002
$U \rightarrow C$	3.4 ± 1.1	3.48	0.02	0.002	0.001
$U \rightarrow O_1 \rightarrow N_2$	3.1 ± 0.7	3.59	0.02	0.004	0.002
$U \rightarrow O_{y1(1)} \rightarrow O_{y1(2)}$	2 ^a	3.60	0.01	0.004	0.001
$U \rightarrow O_{y1(1)} \rightarrow U \rightarrow O_{y1(2)}$	2 ^a	3.60	0.01	0.004	0.001
$U \rightarrow O_{y1(1)} \rightarrow U \rightarrow O_{y1(1)}$	2 ^a	3.60	0.01	0.004	0.001
$U \rightarrow O_{y1} \rightarrow O_1$	6.2 ± 0.5	3.59	0.01	0.003	0.001
$\Delta E_1 = -2 \pm 1 \text{ eV}$					
$\Delta E_2 = -1 \pm 3 \text{ eV}$					

^a The coordination number for $U \rightarrow O_{y1}$ was held at 2 for the model.

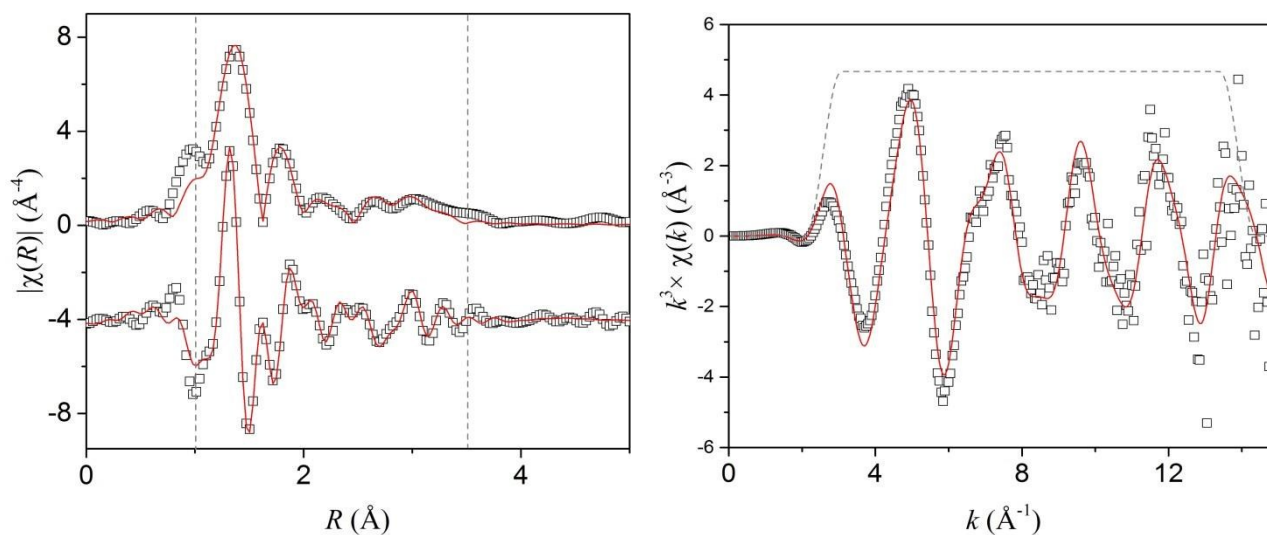


Figure S12 Data (open symbols) and best-fit chelation model (line) for fit of EXAFS data for polymer fibres contacted with seawater simulant containing uranium and vanadium. The Fourier transform is displayed on the left, with the magnitude (top) and real components. The right column is plotted in k -space. All plots are displayed with k^3 -weighting. Grey lines display the fitting window.

5.2.3 *Seawater-Contacted Fibres (As Received)*. The model used to fit the fibre data was composed of several shells of light scattering elements and one transition metal scatterer. The first shell was composed exclusively of the tightly-bound uranyl axial oxygen (O_{yl}) with degeneracy fixed at 2. The second shell was composed of light scatterers at two different distances with equal, but variable degeneracy (O_1, N_1). The third shell was composed of light scatterers at different distances with equal, but variable degeneracy (N_2, C) and a transition metal, Ni. ΔR and σ^2 were free parameters for all direct scattering paths, and degeneracy was a free parameter for all direct scattering paths except O_{yl} . To comply with the Nyquist criterion, the degeneracy and σ^2 for O_1 and N_1 were defined as equivalent, and the degeneracy, ΔR , and σ^2 for N_2 and C were defined as equivalent. Fits with more parameters yielded similar values in R-factor, but much larger χ_v^2 . This model structure is most consistent with an average coordination environment consisting of approximately two chelating ligands per uranyl and one μ^2 bridging Ni, however, the large error for Ni coordination number and σ^2 suggests this model is not able to completely describe the data. It is likely fractional contributions from phosphate, carbonate, and different metal species, are necessary to improve the fit. Data were not fit beyond 3.5 Å in R-space due to the noise in the data.

Table S12 Paths, Initial Path Lengths, Degeneracies, and Parameters for Fitting Polymer Fibres Contacted with Filtered Environmental Seawater for 56 Days

Scattering Path	N_{degen}	$R(\text{\AA})$	$\Delta R(\text{\AA})$	$\sigma^2(\text{\AA}^2)$	ΔE_1
$U \rightarrow O_{y1}$	2	1.79	$\Delta R-O_{y1}$	σ^2-O_{y1}	ΔE_1
$U \rightarrow O_1$	CN_1	2.43	$\Delta R-O$	σ^2-O	ΔE_2
$U \rightarrow N_1$	CN_1	2.56	$\Delta R-O$	σ^2-O	ΔE_2
$U \rightarrow N_2$	CN_2	3.35	$\Delta R-N$	σ^2-N	ΔE_2
$U \rightarrow C$	CN_2	3.48	$\Delta R-N$	σ^2-N	ΔE_2
$U \rightarrow Ni$	CN_3	3.53	$\Delta R-Ni$	σ^2-Ni	ΔE_2
$U \rightarrow O_1 \rightarrow N_2$	CN_2	3.56	$0.5 \times \Delta R-O_1$ $+ 0.5 \times \Delta R-N_2$	$0.5 \times \sigma^2-O$ $+ 0.5 \times \sigma^2-N$	ΔE_2
$U \rightarrow O_{y1(1)} \rightarrow O_{y1(2)}$	2	3.57	$2 \times \Delta R-O_{y1}$	$2 \times \sigma^2-O_{y1}$	ΔE_1
$U \rightarrow O_{y1(1)} \rightarrow U \rightarrow O_{y1(2)}$	2	3.57	$2 \times \Delta R-O_{y1}$	$2 \times \sigma^2-O_{y1}$	ΔE_1
$U \rightarrow O_{y1(1)} \rightarrow U \rightarrow O_{y1(1)}$	2	3.57	$2 \times \Delta R-O_{y1}$	$2 \times \sigma^2-O_{y1}$	ΔE_1
$U \rightarrow O_{y1} \rightarrow N_1$	$2 \times \text{CN}_1$	3.60	$0.5 \times \Delta R-O_{y1}$ $+ 0.5 \times \Delta R-N_1$	$0.5 \times \sigma^2-O_{y1} +$ $0.5 \times \sigma^2-O$	ΔE_1
$U \rightarrow O_{y1} \rightarrow O_1$	$2 \times \text{CN}_1$	3.65	$0.5 \times \Delta R-O_{y1}$ $+ 0.5 \times \Delta R-O_1$	$0.5 \times \sigma^2-O_{y1} +$ $0.5 \times \sigma^2-O$	ΔE_1
$U \rightarrow N_1 \rightarrow C$	$2 \times \text{CN}_2$	3.70	$0.5 \times \Delta R-N_1$ $+ 0.5 \times \Delta R-C$	$0.5 \times \sigma^2-O +$ $0.5 \times \sigma^2-N$	ΔE_2

Table S13 Best Fit Values for Polymer Fibres Contacted with Filtered Environmental Seawater

Scattering Path	N_{degen}	$R(\text{\AA})$	error	$\sigma^2 (\text{\AA}^2)$	error
$U \rightarrow O_{yl}$	2 ^a	1.80	0.01	0.002	< 0.001
$U \rightarrow O_1$	2.8 ± 0.6	2.40	0.02	0.003	0.002
$U \rightarrow N_1$	2.8 ± 0.6	2.56	0.02	0.003	0.002
$U \rightarrow N_2$	2.8 ± 0.2^b	3.41	0.07	0.003	0.002
$U \rightarrow C$	2.8 ± 0.2^b	3.54	0.07	0.003	0.002
$U \rightarrow Ni$	1 ± 1	3.41	0.04	0.006	0.004
$U \rightarrow O_1 \rightarrow N_2$	2.8 ± 0.3	3.59	0.04	0.004	0.002
$U \rightarrow O_{yl(1)} \rightarrow O_{yl(2)}$	2 ^a	3.61	0.01	0.004	0.001
$U \rightarrow O_{yl(1)} \rightarrow U \rightarrow O_{yl(2)}$	2 ^a	3.61	0.01	0.004	0.001
$U \rightarrow O_{yl(1)} \rightarrow U \rightarrow O_{yl(1)}$	2 ^a	3.61	0.01	0.004	0.001
$U \rightarrow O_{yl} \rightarrow N_1$	5.6 ± 0.3	3.70	0.01	0.004	0.001
$U \rightarrow O_{yl} \rightarrow O_1$	5.6 ± 0.3	3.70	0.01	0.003	0.001
$U \rightarrow N_1 \rightarrow C$	5.6 ± 0.3	3.72	0.04	0.003	0.002
$\Delta E_1 = 0 \pm 1 \text{ eV}$					
$\Delta E_2 = 2 \pm 2 \text{ eV}$					

^a The coordination number for $U \rightarrow O_{yl}$ was held at 2 for the model.

^b The uncertainty in step height during normalization can be as large as 10%. As S_0^2 , N , and step height are all components of the amplitude, the coordination number cannot be determined to greater accuracy than 10%.¹⁸

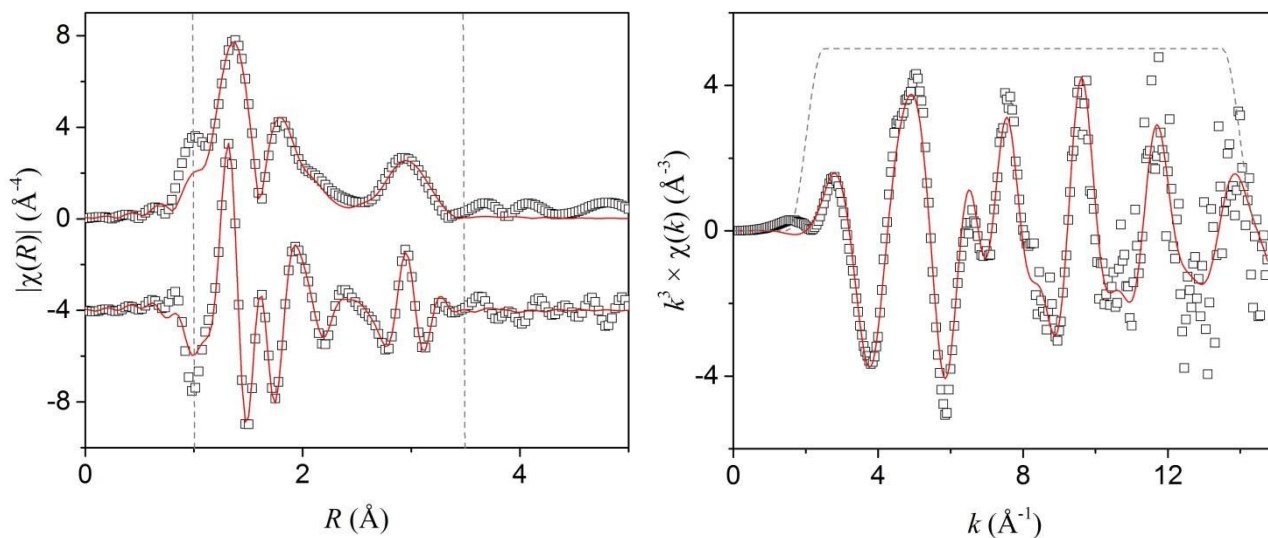


Figure S13 Data (open symbols) and best-fit chelation model (line) for fit of EXAFS data for polymer fibres contacted with filtered environmental seawater for 56 days. The Fourier transform is displayed on the left, with the magnitude (top) and real components. The right column is plotted in k -space. All plots are displayed with k^3 -weighting. Grey lines display the fitting window.

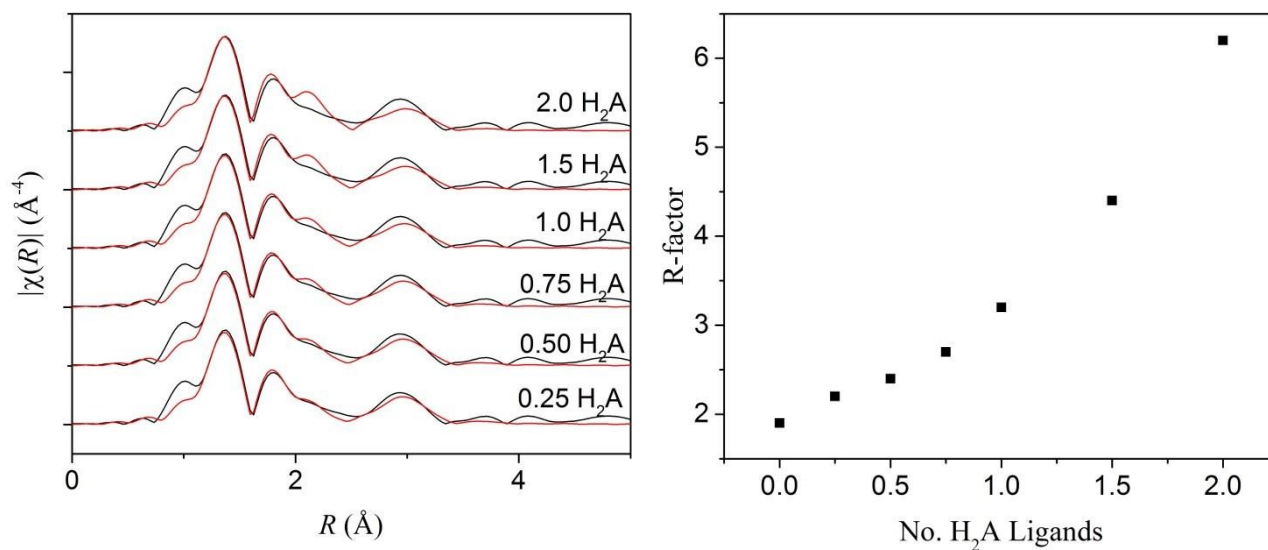


Figure S14 Influence of cyclic imide dioxime (abbreviated in this figure as H_2A^7) on fit of EXAFS data for seawater-contacted polymer fibres. (Left) Including the imide nitrogen of the tridentate-binding model results in a visibly worse fit with increasing contribution. (Right) R-factor as a function of number

of cyclic imide dioxime ligands included in the average fit. These R-factors correspond to the plots displayed in the left panel.

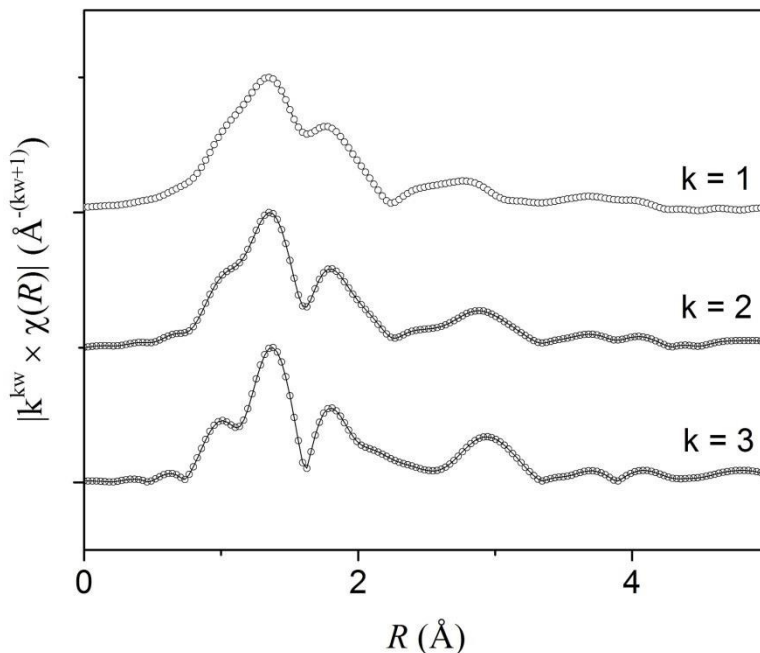


Figure S15 EXAFS spectra for seawater-contacted polymer fibers displayed with k-weights of 1, 2, and 3. The increasing contribution of the feature at 3 Å at higher k-weighting is consistent with scattering from a higher Z-number element. All spectra were collected at room temperature.

5.2.4 Seawater-Contacted Fibres (Post-Elution). The data collected for seawater contacted fibres post-elution is significantly more noisy than any of the previously discussed samples. As a result, a smaller amount of data were used to perform the fit, restricting the number of parameters which could be used and directly impacting the fit metrics. The model used to fit the fibre data was constructed in a similar fashion to the simulant-contacted fibres. The first shell was composed exclusively of the tightly-bound uranyl axial oxygen (O_{y1}) with degeneracy fixed at 2. The second shell was composed of light scatterers at two different distances with equal, but variable degeneracy (O_1, N_1). The third shell was composed of light scatterers with variable degeneracy (N_2, C). ΔR and σ^2 were free parameters for all

direct scattering paths. Degeneracy was a free parameter for all direct scattering paths except O_{yl} . To comply with the Nyquist criterion, the degeneracy and σ^2 for O_1 and N_1 were defined as equivalent, and the degeneracy, ΔR , and σ^2 for N_2 and C were defined as equivalent. Data were not fit beyond 3.5 Å in R-space due to the noise in the data.

Table S14 Paths, Initial Path Lengths, Initial Degeneracies, and Parameters for Fitting Polymer Fibres Contacted Environmental Seawater and Eluted with Dilute HCl

Scattering Path	N_{degen}	$R(\text{Å})$	$\Delta R(\text{Å})$	$\sigma^2(\text{Å}^2)$	ΔE_1
$U \rightarrow O_{yl}$	2	1.79	$\Delta R - O_{yl}$	$\sigma^2 - O_{yl}$	ΔE_1
$U \rightarrow O_1$	CN_1	2.43	$\Delta R - O$	$\sigma^2 - O$	ΔE_2
$U \rightarrow N_1$	CN_1	2.53	$\Delta R - O$	$\sigma^2 - O$	ΔE_2
$U \rightarrow N_2$	CN_2	3.36	$\Delta R - N$	$\sigma^2 - N$	ΔE_2
$U \rightarrow C$	CN_2	3.47	$\Delta R - C$	$\sigma^2 - C$	ΔE_2
$U \rightarrow O_1 \rightarrow N_2$	CN_2	3.57	$0.5 \times \Delta R - O_1$ $+ 0.5 \times \Delta R - N_2$	$0.5 \times \sigma^2 - O$ $+ 0.5 \times \sigma^2 - N$	ΔE_2
$U \rightarrow O_{yl(1)} \rightarrow O_{yl(2)}$	2	3.57	$2 \times \Delta R - O_{yl}$	$2 \times \sigma^2 - O_{yl}$	ΔE_1
$U \rightarrow O_{yl(1)} \rightarrow U \rightarrow O_{yl(2)}$	2	3.57	$2 \times \Delta R - O_{yl}$	$2 \times \sigma^2 - O_{yl}$	ΔE_1
$U \rightarrow O_{yl(1)} \rightarrow U \rightarrow O_{yl(1)}$	2	3.57	$2 \times \Delta R - O_{yl}$	$2 \times \sigma^2 - O_{yl}$	ΔE_1
$U \rightarrow O_1 \rightarrow N_1$	$2 \times \text{CN}_1$	3.67	$0.5 \times \Delta R - O_1$ $+ 0.5 \times \Delta R - N_1$	$0.5 \times \sigma^2 - O_{yl} +$ $0.5 \times \sigma^2 - O$	ΔE_2

Table S15 Best Fit Values for Polymer Fibres Contacted with Filtered Environmental Seawater and Eluted with Dilute HCl

Scattering Path	N_{degen}	$R(\text{\AA})$	error	$\sigma^2 (\text{\AA}^2)$	error
$U \rightarrow O_{y1}$	2 ^a	1.80	0.01	0.002	< 0.001
$U \rightarrow O_1$	3.0 ± 1.2	2.38	0.02	0.006	0.006
$U \rightarrow N_1$	3.0 ± 1.2	2.51	0.02	0.006	0.006
$U \rightarrow N_2$	3.0 ± 0.3	3.38	0.04	0.006	0.004
$U \rightarrow C$	3.0 ± 0.3	3.49	0.02	0.006	0.004
$U \rightarrow O_1 \rightarrow N_2$	3.0 ± 0.3	3.56	0.02	0.006	0.004
$U \rightarrow O_{y1(1)} \rightarrow O_{y1(2)}$	2 ^a	3.61	0.01	0.004	0.001
$U \rightarrow O_{y1(1)} \rightarrow U \rightarrow O_{y1(2)}$	2 ^a	3.61	0.01	0.004	0.001
$U \rightarrow O_{y1(1)} \rightarrow U \rightarrow O_{y1(1)}$	2 ^a	3.61	0.01	0.004	0.001
$U \rightarrow O_1 \rightarrow N_1$	6.0 ± 2.4	3.65	0.01	0.006	0.006
$\Delta E_1 = 4 \pm 2 \text{ eV}$					
$\Delta E_2 = 0 \pm 4 \text{ eV}$					

^a The coordination number for $U \rightarrow O_{y1}$ was held at 2 for the model.

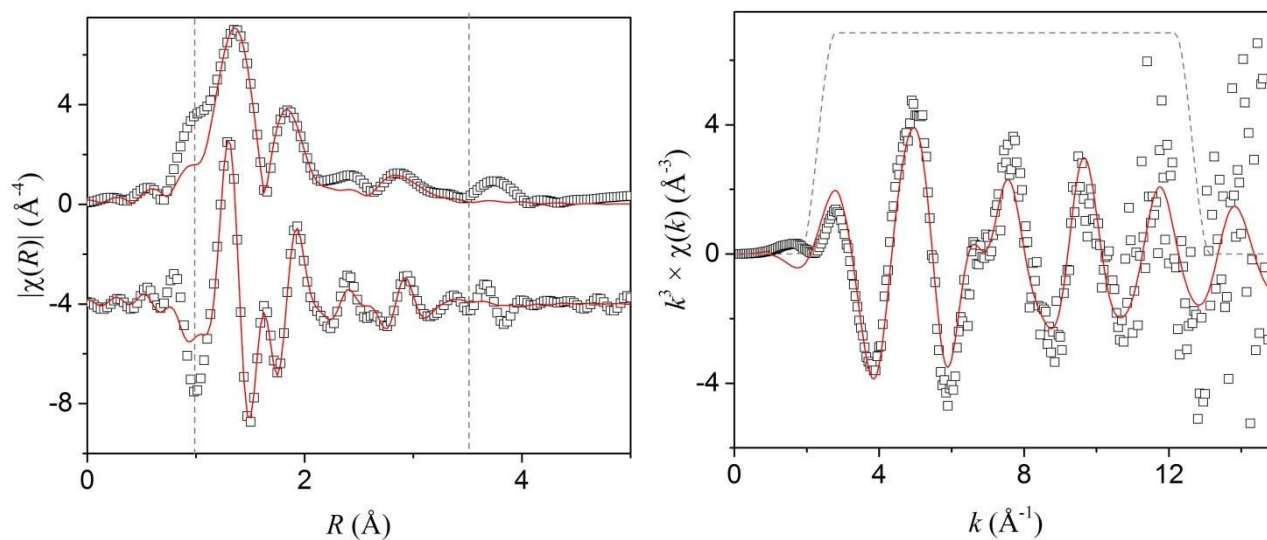


Figure S16 Data (open symbols) and best-fit chelation model (line) for fit of EXAFS data for polymer fibres contacted with filtered environmental seawater for 56 days, then eluted with dilute HCl. The Fourier transform is displayed on the left, with the magnitude (top) and real components. The right

column is plotted in k-space. All plots are displayed with k^3 -weighting. Grey lines display the fitting window.

6 X-ray Photoelectron Spectroscopy

Polyethylene pellets were hot-pressed to generate a polyethylene film. The film was then grafted by irradiation graft polymerization (RIGP) as previously reported for the fibrous adsorbent. (REF 39 of manuscript) The polyethylene film was then contacted with a brine containing 6-8 ppm uranium as uranyl nitrate hexahydrate (17 mg, 0.034 mmol) with sodium chloride (25.6 g, 0.44 mol) and sodium bicarbonate (194 mg, 2.3 mmol) in 1 L of deionized water. This affords a uranyl brine that contains the seawater relevant concentrations of sodium chloride and bicarbonate while increasing the amount of uranium to enhance the sorption kinetics. X-ray photoelectron spectroscopy (XPS) data were collected using a PHI 3056 spectrometer with an Al anode source operated at 15 kV and an applied power of 350 W. Adventitious carbon was used to calibrate the binding energy shifts of the sample $C1s = 284.8$ eV. High resolution data was collected at pass energy of 5.85 eV with 0.05 eV step sizes and a minimum of 60 scans to improve the signal to noise ratio; lower resolution survey scans were collected at pass energy of 93.5 eV with 0.5 eV step sizes and a minimum of 25 scans.

The collected XPS data from the grafted polyethylene film is shown in Figure S13. The surface consisted of 5 at% N, 2.5 at% Na, 0.6 at% U, 8.9 at% O, 27.0% F, with the balance carbon. The primary U $4f_{7/2}$ species has a binding energy of 381.6 eV which is attributed to an U^{6+} species adsorbed from solution.²¹ There is a second higher energy U 4f species located at 384.2 eV likely due to U^{6+} -OH or U^{6+} -O-Na. The N1s data shows the presence of two N species. The first species with a binding energy of 398.7 eV is due to a $H_2N-C=N-OH$ iminic nitrogen. The second species, 399.7 eV, is due to the $H_2N-C=N-OH$ nitrogen.^{22, 23}

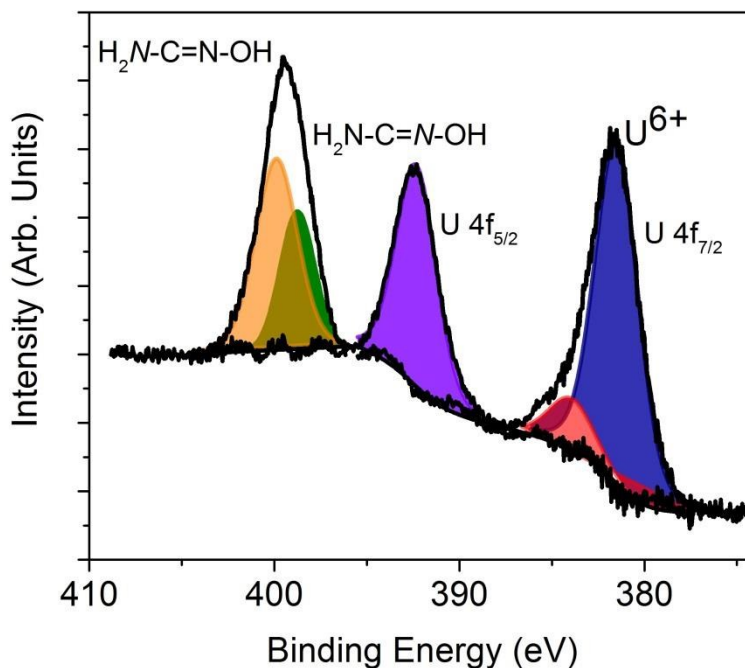


Figure S17 XPS spectra and fit for poly-acetamidoxime film saturated with uranyl in DI water.

7. Differential Pair Distribution Function

Pair distribution spectra (PDF) were obtained on samples cryogenically pulverized as discussed in section 3.1. Powdered samples were packed in a Kapton tube approximately 15 mm in length and 0.0320" ID. Each end of the tube was sealed with epoxy. This sealed tube was then placed in a second Kapton tube, approximately 20 mm in length and 0.0395" ID. Again, each end was sealed with epoxy. This manner of secondary containment was sufficient for measurement of radiological samples at the Advanced Photon Source. Data were collected at 58.88 keV on beamline 11ID-B. The detector was positioned 19.556 cm from the sample as determined by calibration against a CeO₂ standard. Three data sets were obtained for each sample, consisting of 100 frames each, collected over 3 seconds per frame. Raw images were processed using Fit-2D²⁴ and PDFs were extracted as discussed elsewhere.²⁵

Differential pair distribution function (d-PDF) analysis was performed, where the difference between two PDF spectra is obtained through direct subtraction of the reference PDF spectrum (Figure S18).²⁶ Using the pristine adsorbent as a reference PDF spectrum, d-PDF spectra were obtained for both

seawater-contacted fibres and HCl-eluted fibres. The d-PDF spectrum was also obtained between the seawater-contacted fibres and the HCl-eluted fibres.

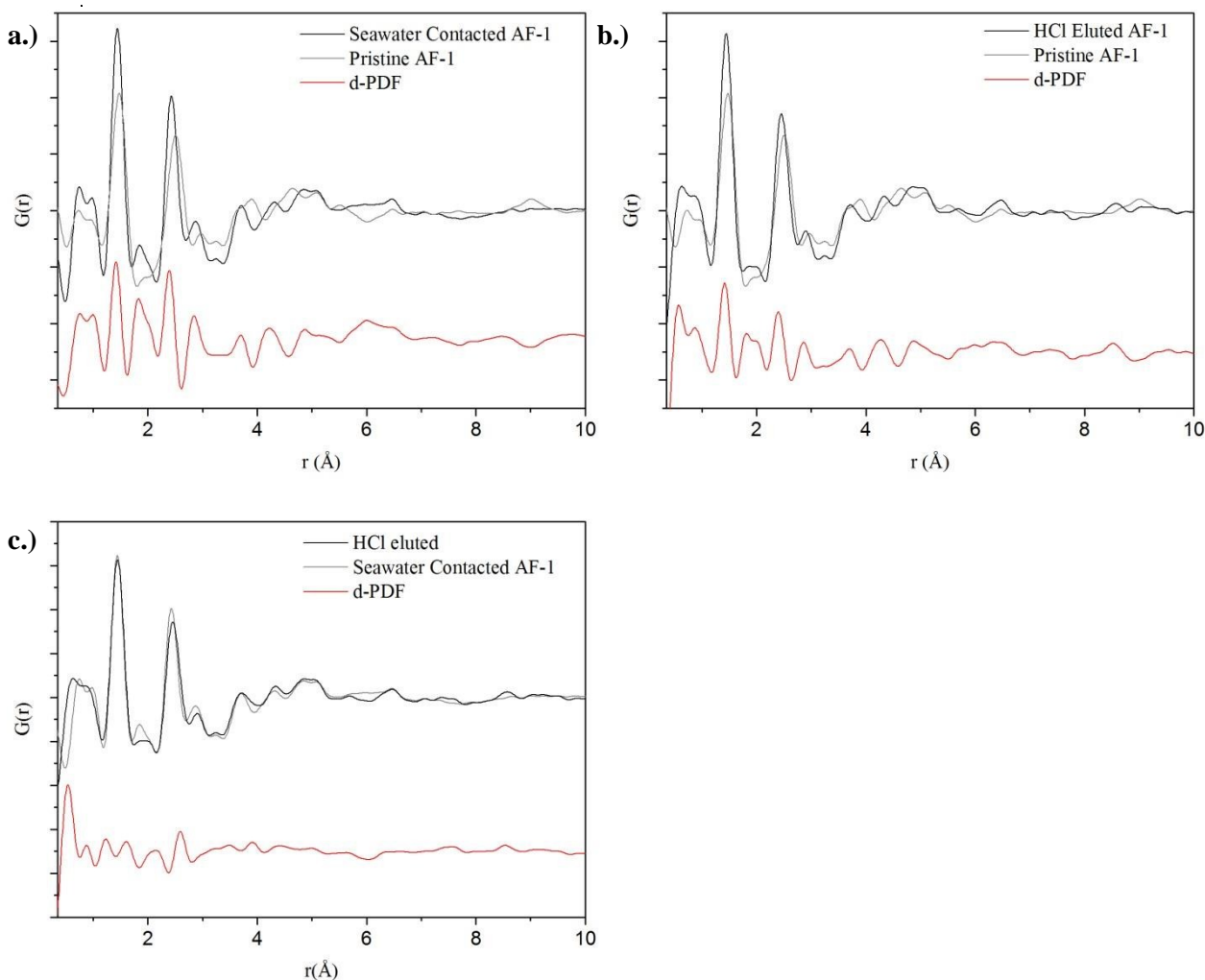


Figure S18 PDF and d-PDF spectra for amidoxime-functionalized fibres. Plot a) displays the d-PDF between seawater-contacted fibers and pristine fibres, while b) displays the d-PDF for HCl-eluted fibres and pristine fibres. Plot c) presents the d-PDF between HCl-eluted fibres and seawater-contacted fibres. In all instances, the reference spectra is plotted in grey and is subtracted from the spectra plotted in black to obtain the d-PDF spectra, plotted in red.

Analysis of d-PDF spectra for both seawater-contacted fibres and HCl-eluted fibres reveal the most significant probability differences occur at bond lengths of 1.5, 1.8, 2.5, and 3 Å. It is encouraging that the distance between U-O_{yl} is approximately 1.8 Å, the distance between U and the first shell scatterers is approximately 2.5 Å, and a feature is apparent at approximately 3.5 Å where XAFS fits suggest the presence of a μ^2 -oxo bridged transition metal. Moreover, these features are largely absent in

the d-PDF between seawater-contacted and HCl-eluted fibres, consistent with an amidoxime-bound uranium and an eluted transition metal. Nevertheless, definitive identification of structural features is not possible, due to the large number of metals bound by the seawater contacted fibres (see Table S2). The increased bond length probability can also be attributed to interactions with transition metals that are not eluted with HCl (specifically V and Cu), as well as the alkali and alkali earth cations (Na, Mg, Ca) which are ubiquitous in seawater.^{2,4}

8. Computational

8.1. Methods

Density functional theory (DFT) calculations were carried out using the Gaussian 09 Revision D.01.²⁷ Moller-Plesset perturbation theory (MP2)^{28, 29} and coupled-cluster theory calculations with singles, doubles, and perturbative triples excitations (CCSD(T))³⁰⁻³² were performed with the NWChem 6.5 software package.³³ The standard Stuttgart small-core (SSC) 1997 relativistic effective core potential (RECP) was used for uranium, replacing 60 core electrons to account for scalar relativistic effects.³⁴ The valence electrons in this basis set are represented by a contracted [8s/7p/6d/4f] basis. The most diffuse function on uranium (exponent 0.005) was removed to improve SCF convergence. The basis set for the light atoms was 6-311++G(d,p) and aug-cc-pVDZ in DFT and post-Hartree-Fock methods, respectively. Geometry optimizations were performed at the MP2 and B3LYP levels.^{28, 29, 35, 36} Single-point CCSD(T)/SSC/aug-cc-pVDZ calculations using B3LYP/SSC/6-311++G(d,p) and MP2/SSC/aug-cc-pVDZ geometries were employed to determine the benchmark relative energies of UO_2^{2+} complexes with formamidoxime in the η^2 and chelate binding motifs and to determine the sensitivity of the CCSD(T) relative energies to changes in geometries of uranyl complexes at different level of theories. Only the valence electrons were correlated in the MP2 and CCSD(T) calculations. Frequency calculations were performed at the B3LYP/SSC/6-31+G(d) level to verify that geometries were minima and to compute zero point energies and thermal corrections using the rigid rotor-harmonic oscillator approximation, except that vibrational frequencies lower than 60 cm^{-1} were raised to 60 cm^{-1} . This procedure is similar to that proposed by Truhlar and co-workers³⁷ to correct for the well-known breakdown of the harmonic

oscillator model for the free energies of low-frequency vibrational modes. Using the gas phase geometries, implicit solvent corrections were obtained at the B3LYP/SSC/6-31+G(d) level using the IEF-PCM³⁸⁻⁴⁰ solvation model in Gaussian.²⁷ Since only the first coordination shell was treated explicitly in this study, it was possible to perform a systematic search of low-energy clusters for a given composition. The results are reported using the lowest energy clusters identified at the B3LYP/SSC/6-311++G(d,p) level for a given stoichiometry and binding motif.

8.2. Analysis of the computational results

In this work, we employ high level coupled-cluster CCSD(T)/aug-cc-pVDZ calculations to investigate the potential binding motifs of uranyl complexes with formamidoxime ligands. The chosen ligand is small enough that high-level *ab initio* calculations can be readily performed. Relative energies obtained from CCSD(T) calculations are used as benchmarks against DFT and MP2 predicted energies. The most stable five- and six-coordinate B3LYP geometries of the uranyl complexes with 1–3 ligands involving η^2 -binding with the N-O bond and chelation through the oxime oxygen and amine nitrogen donor atoms are shown in Figure S14. Consistent with previous DFT calculations and X-ray diffraction data,^{1, 5, 41} the η^2 binding motif is the most stable at the B3LYP and MP2 levels for all amidoxime complexes. The results given in Table S16 indicate that the presence of one chelate motif destabilized the complex by 2.8–5.1 kcal/mol at the B3LYP and by 1.9–4.7 kcal/mol at the MP2 level. However, after the application of the CCSD(T) correction, the difference in energy between the two binding forms becomes much smaller. In particular, a five-coordinate 1:2 uranyl complex with a mixed coordination of the two ligands, $[\text{UO}_2(\text{ao-}\eta^2)(\text{ao-chelate})(\text{H}_2\text{O})]$ is slightly more stable than that with pure η^2 coordination, $[\text{UO}_2(\text{ao-}\eta^2)_2(\text{H}_2\text{O})]$ at the CCSD(T) level. The high consistency of the CCSD(T) results obtained with B3LYP and MP2 geometries (within 0.4 kcal/mol of each other) indicates that the CCSD(T) relative energies are not particularly sensitive to the choice of the geometry obtained at different levels of theory. In summary, analysis of the relative stabilities of uranyl complexes with amidoxime with the effect of higher order correlation estimated at the coupled-cluster theory reveals that the difference in the stability

of the η^2 and chelate binding motifs is smaller than previously thought based on DFT calculations⁵ and both forms may coexist in thermodynamic equilibrium in aqueous solution.

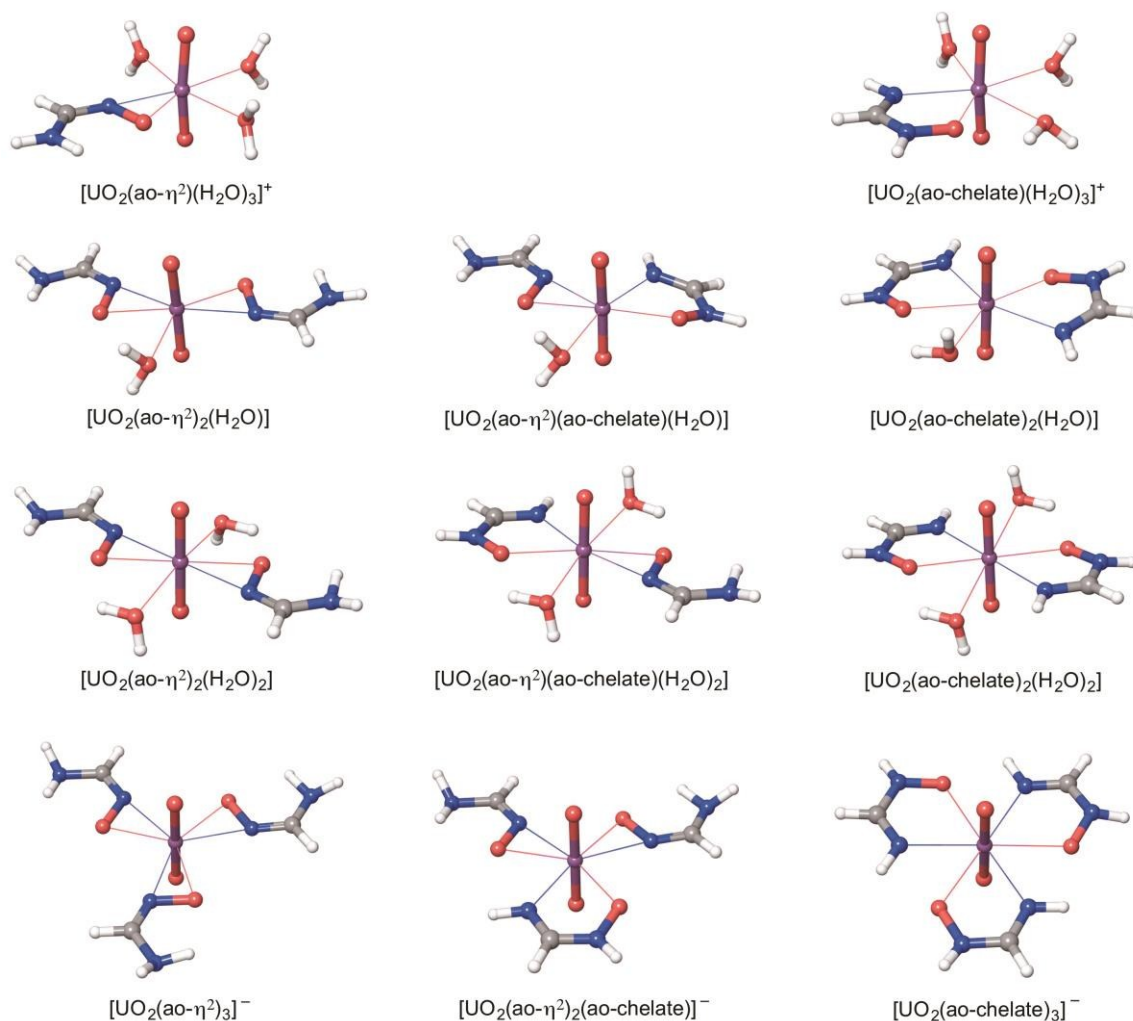


Figure S19. Structures of uranyl complexes with formamidoxime (ao), $[\text{UO}_2(\text{ao})_x(\text{H}_2\text{O})_y]^{2-x}$, obtained after geometry optimization at the B3LYP/SSC/6-311++G(d,p) level of theory.

Table S16. Relative stabilities of $[\text{UO}_2(\text{ao})_x(\text{H}_2\text{O})_y]^{2-x}$ complexes obtained in the solvent reaction field at several levels of theory (ΔG_{aq} in kcal/mol).^a Structures of the representative complexes are shown in Figure S16.

stoichiometry/binding mode	B3LYP ^b	MP2 ^c	CCSD(T)// B3LYP ^d	CCSD(T)// MP2 ^d
$[\text{UO}_2(\text{ao-}\eta^2)(\text{H}_2\text{O})_3]^+$	0.00	0.00	0.00	0.00

$[\text{UO}_2(\text{ao-chelate})(\text{H}_2\text{O})_3]^+$	5.10	3.27	1.23	0.96
$[\text{UO}_2(\text{ao-}\eta^2)_2(\text{H}_2\text{O})]$	0.00	0.00	0.34	0.03
$[\text{UO}_2(\text{ao-}\eta^2)(\text{ao-chelate})(\text{H}_2\text{O})]$	3.07	1.93	0.00	0.00
$[\text{UO}_2(\text{ao-chelate})_2(\text{H}_2\text{O})]$	9.03	7.21	3.48	3.16
$[\text{UO}_2(\text{ao-}\eta^2)_2(\text{H}_2\text{O})_2]$	0.00	0.00	0.00	0.00
$[\text{UO}_2(\text{ao-}\eta^2)(\text{ao-chelate})(\text{H}_2\text{O})_2]$	4.96	4.67	2.85	2.92
$[\text{UO}_2(\text{ao-chelate})_2(\text{H}_2\text{O})_2]$	13.5	13.9	10.1	10.3
$[\text{UO}_2(\text{ao-}\eta^2)_3]^-$	0.00	0.00	0.00	0.0
$[\text{UO}_2(\text{ao-}\eta^2)_2(\text{ao-chelate})]^-$	2.84	2.17	1.28	1.32
$[\text{UO}_2(\text{ao-}\eta^2)(\text{ao-chelate})_2]^-$	9.31	8.15	6.19	6.34
$[\text{UO}_2(\text{ao-chelate})_3]^-$	21.3	21.6	17.8	18.2

^aZero point energies, thermal corrections, and solvent corrections using the IEF-PCM solvation model were calculated at the B3LYP/SSC/6-31+G(d) level. ^bB3LYP/SSC/6-311++G(d,p). ^cMP2/SSC/aug-cc-pVDZ. ^dSingle-point CCSD(T)/SSC/aug-cc-pVDZ energies on either B3LYP/SSC/6-311++G(d,p) or MP2/SSC/aug-cc-pVDZ optimized geometries.

9. Crystallography

Single crystal X-ray diffraction of uranyl benzamidoxime was performed with a Bruker D8 Venture, dual microsource (Cu and Mo) diffractometer with a CMOS detector. Mo $K\alpha$ radiation was used. The frames were integrated with the Bruker SAINT© build in the APEX II software package using a narrow-frame integration algorithm, which also corrects for the Lorentz and polarization effects. Absorption corrections were applied using SADABS. Structures were solved by direct methods and refined to convergence by the least squares method on F^2 using the SHELXTL-2013 software suite.⁴² All non-hydrogen atoms were refined anisotropically except for the solvent molecule. The crystal structure is available from the Cambridge Crystallographic Database, number 1419942.

Table S17. Crystallographic information.

Name	Uranyl Benzamidoxime
Formula	UC16H22N4O6
Fw	604.41
Temperature (K)	100.0
Wavelength (Å)	0.71073
Crystal system	monoclinic
Space group	$P2_1/c$
a , Å	10.4376(8)
b , Å	5.7148(4)
c , Å	15.9916(11)
α , °	90
β , °	102.543(2)
γ , °	90
V , Å ³	931.11(12)
Z	2
Density (calcd. g/cm ³)	2.156
Absorption coeff. (mm ⁻¹)	8.758
F(000)	572
θ range data collection	2.610 – 27.155
Limiting indices	$-13 \leq h \leq 13$ $-7 \leq k \leq 7$ $-20 \leq l \leq 20$
Reflection collected	11878
Independent reflections	2068
R(int)	0.0685
Data/restraints/parameters	2068/1/129
Goodness-of-fit on F^2	1.043
Final R indices [$I > 2\sigma(I)$]	R1 = 0.0288, wR2 = 0.0485
R indices (all data)	R1 = 0.0613, wR2 = 0.0550

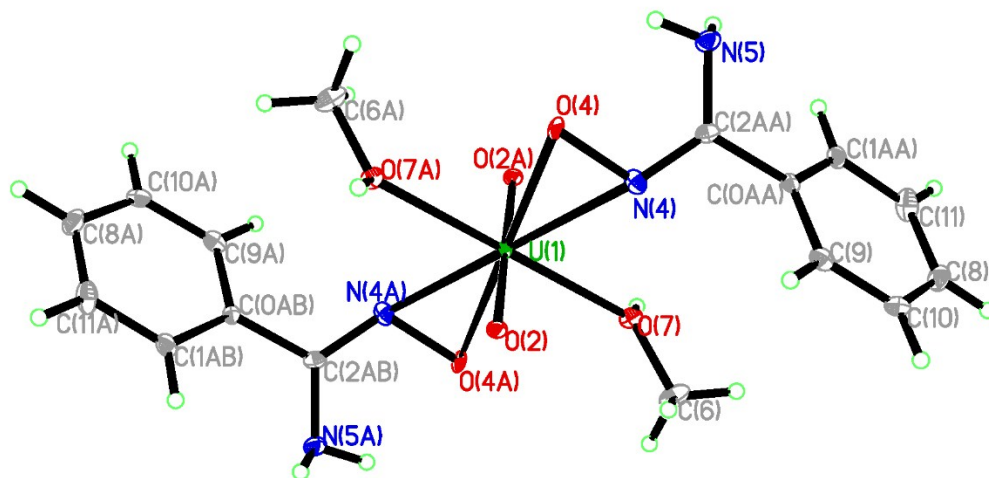


Figure S20. ORTEP of Uranyl Benzamidoxime at 50% probability.

10. References

1. S. P. Kelley, P. S. Barber, P. H. K. Mullins and R. D. Rogers, *Chem. Commun.*, 2014, **50**, 12504-12507.
2. J. Kim, C. Tsouris, R. T. Mayes, Y. Oyola, T. Saito, C. J. Janke, S. Dai, E. Schneider and D. Sachde, *Sep. Sci. Technol.*, 2013, **48**, 367-387.
3. J. Kim, Y. Oyola, C. Tsouris, C. R. Hexel, R. T. Mayes, C. J. Janke and S. Dai, *Ind. Eng. Chem. Res.*, 2013, **52**, 9433-9440.
4. J. Kim, C. Tsouris, Y. Oyola, C. J. Janke, R. T. Mayes, S. Dai, G. Gill, L.-J. Kuo, J. Wood, K.-Y. Choe, E. Schneider and H. Lindner, *Ind. Eng. Chem. Res.*, 2014, **53**, 6076-6083.
5. S. Vukovic, L. A. Watson, S. O. Kang, R. Custelcean and B. P. Hay, *Inorg. Chem.*, 2012, **51**, 3855-3859.
6. *US Pat.*, 2009.
7. G. Tian, S. Teat, Z. Zhang and L. Rao, *Dalton. Trans.*, 2012, **41**, 11579-11586.
8. S. O. Kang, S. Vukovic, R. Custelcean and B. P. Hay, *Ind. Eng. Chem. Res.*, 2012, **51**, 6619-6624.
9. A. Zhang, T. Asakura and G. Uchiyama, *React. Funct. Polym.*, 2003, **57**, 67-76.
10. S. Katragadda, H. D. Gesser and A. Chow, *Talanta*, 1997, **45**, 257-263.
11. A. Zhang, G. Uchiyama and T. Asakura, *Sep. Sci. Technol.*, 2003, **38**, 1829-1849.
12. N. Seko, A. Katakai, M. Tamada, T. Sugo and F. Yoshii, *Sep. Sci. Technol.*, 2004, **39**, 3753-3767.
13. T. Suzuki, K. Saito, T. Sugo, H. Ogura and K. Oguma, *Anal. Sci.*, 2000, **16**, 429-432.
14. B. L. Henke, E. M. Gullikson and J. C. Davis, *At. Data Nucl. Data Tables*, 1993, **54**, 181-342.
15. B. Ravel and M. Newville, *J. Synchrotron Radiat.*, 2005, **12**, 537-541.
16. J. J. Rehr and R. C. Albers, *Rev. Mod. Phys.*, 2000, **72**, 621-654.
17. S. D. Kelly, D. Hesterberg and B. Ravel, in *Methods of Soil Analysis*, eds. A. L. Ulery and L. R. Drees, Soil Science Society of America, Madison, WI, 2008, vol. 5, ch. 14, pp. 387 - 463.
18. S. D. Kelly, K. M. Kemner, J. B. Fein, D. A. Fowle, M. I. Boyanov, B. A. Bunker and N. Yee, *Geochim. Cosmochim. Acta*, 2002, **66**, 3855-3871.
19. S. Calvin, *XAFS for Everyone*, CRC Press, Boca Raton, FL, 2013.

20. C. Den Auwer, E. Simoni, S. Conradson and C. Madic, *Eur. J. Inorg. Chem.*, 2003, **2003**, 3843-3859.
21. E. S. Ilton and P. S. Bagus, *Surf. Interface Anal.*, 2011, **43**, 1549-1560.
22. J. Gorka, R. T. Mayes, L. Baggetto, G. M. Veith and S. Dai, *J. Mater. Chem. A*, 2013, **1**, 3016-3026.
23. H.-w. Yu, S.-s. Yang, H.-m. Ruan, J.-n. Shen, C.-j. Gao and B. Van der Bruggen, *Appl. Clay Sci.*, 2015, **111**, 67-75.
24. A. P. Hammersley, S. O. Svensson, M. Hanfland, A. N. Fitch and D. Hausermann, *High Pressure Research*, 1996, **14**, 235-248.
25. P. J. Chupas, X. Qiu, J. C. Hanson, P. L. Lee, C. P. Grey and S. J. L. Billinge, *J. Appl. Crystallogr.*, 2003, **36**, 1342-1347.
26. K. W. Chapman, P. J. Chupas and C. J. Kepert, *J. Am. Chem. Soc.*, 2005, **127**, 11232-11233.
27. M. J. Frisch, G. W. Trucks, H. B. Schlegel, G. E. Scuseria, M. A. Robb, J. R. Cheeseman, G. Scalmani, V. Barone, B. Mennucci, G. A. Petersson, H. Nakatsuji, M. Caricato, X. Li, H. P. Hratchian, A. F. Izmaylov, J. Bloino, G. Zheng, J. L. Sonnenberg, M. Hada, M. Ehara, K. Toyota, R. Fukuda, J. Hasegawa, M. Ishida, T. Nakajima, Y. Honda, O. Kitao, H. Nakai, T. Vreven, J. A. Montgomery, Jr. , J. E. Peralta, F. Ogliaro, M. Bearpark, J. J. Heyd, E. Brothers, K. N. Kudin, V. N. Staroverov, R. Kobayashi, J. Normand, K. Raghavachari, A. Rendell, J. C. Burant, S. S. Iyengar, J. Tomasi, M. Cossi, N. Rega, M. J. Millam, M. Klene, J. E. Knox, J. B. Cross, V. Bakken, C. Adamo, J. Jaramillo, R. Gomperts, R. E. Stratmann, O. Yazyev, A. J. Austin, R. Cammi, C. Pomelli, J. W. Ochterski, R. L. Martin, K. Morokuma, V. G. Zakrzewski, G. A. Voth, P. Salvador, J. J. Dannenberg, S. Dapprich, A. D. Daniels, Ö. Farkas, J. B. Foresman, J. V. Ortiz, J. Cioslowski and D. J. Fox, *Journal*, 2009.
28. C. Møller and M. S. Plesset, *Physical Review*, 1934, **46**, 618-622.
29. M. Head-Gordon, J. A. Pople and M. J. Frisch, *Chem. Phys. Lett.*, 1988, **153**, 503-506.
30. G. D. Purvis and R. J. Bartlett, *J. Chem. Phys.*, 1982, **76**, 1910-1918.
31. K. Raghavachari, G. W. Trucks, J. A. Pople and M. Head-Gordon, *Chem. Phys. Lett.*, 1989, **157**, 479-483.
32. J. D. Watts, J. Gauss and R. J. Bartlett, *J. Chem. Phys.*, 1993, **98**, 8718-8733.
33. M. Valiev, E. J. Bylaska, N. Govind, K. Kowalski, T. P. Straatsma, H. J. J. Van Dam, D. Wang, J. Nieplocha, E. Apra, T. L. Windus and W. A. de Jong, *Comput. Phys. Commun.*, 2010, **181**, 1477-1489.
34. M. Dolg, H. Stoll, H. Preuss and R. M. Pitzer, *J. Phys. Chem.*, 1993, **97**, 5852-5859.
35. A. D. Becke, *J. Chem. Phys.*, 1993, **98**, 5648-5652.
36. C. Lee, W. Yang and R. G. Parr, *Phys. Rev. [Sect.] B*, 1988, **37**, 785-789.
37. R. F. Ribeiro, A. V. Marenich, C. J. Cramer and D. G. Truhlar, *J. Phys. Chem. B*, 2011, **115**, 14556-14562.
38. S. Miertuš, E. Scrocco and J. Tomasi, *Chem. Phys.*, 1981, **55**, 117-129.
39. E. Cancès, B. Mennucci and J. Tomasi, *J. Chem. Phys.*, 1997, **107**, 3032-3041.
40. B. Mennucci, E. Cancès and J. Tomasi, *J. Phys. Chem. B*, 1997, **101**, 10506-10517.
41. P. S. Barber, S. P. Kelley and R. D. Rogers, *RSC Adv.*, 2012, **2**, 8526-8530.
42. G. Sheldrick, *Acta Crystallogr. Sect. A: Found. Crystallogr.*, 2008, **64**, 112-122.